Evaluation of Compton Camera Imaging during Boron Neutron Capture Therapy

Luca Christopher Stockhausen

Department of Physics

University of Liverpool

A thesis submitted for the degree of

MPhys

May 2012

Abstract

Boron Neutron Capture Therapy (BNCT) is an advanced dual approach to treating cancer in humans. In BNCT a non-toxic boron-containing compound is intravenously injected into the patient and accumulates in the tumour to be treated. A beam of low-energy neutrons is then directed at the tumour containing the boron (^{10}B) compound. In the tumour, the boron atoms capture the neutrons and split into two new atoms. This releases locally high energy that kills the tumour cell and is usually accompanied by the release of γ-radiation. This project evaluated the feasibility of using a Compton camera detector system to analyse this γ-radiation to produce an image of the region being treated. It has been shown that spectroscopy of ^{10}B is possible, but the image reconstruction is not efficient for small volumes in the short time period required for clinical treatment.

To my parents

Acknowledgements

I would like to acknowledge my supervisors Dr Andrew Boston and Prof Robert Page for all their assistance and help throughout this project. Special thanks to Dr Dan Judson for his help with the simulation programs. I would also like to thank my family and friends for all their support throughout my studies.

Contents

List of Figures

List of Tables

1

Introduction

Global cancer rates increase significantly every year. Some cancers are treatable with chemotherapy alone, while others need radiotherapy and sometimes surgery. Chemotherapy and radiotherapy are two different types of treatment and used in different ways. Chemotherapy refers to the treatment with drugs aiming to stop the cancer cells from reproducing and dividing. It is usually given in a series of sessions before an operation to shrink the tumour and weaken its attachment and is also used to destroy left over cells after an operation. As with any type of medication, there are side effects and healthy tissue can be damaged. Radiotherapy is less severe than chemotherapy. It uses radiation to destroy the cancer cells in a specific spot by damaging the DNA of cancerous cells. The radiation can be directly applied to the tumour instead of injecting drugs into the blood vessels. Up to now, γ-rays were often utilized, but recently carbon ions and protons have been used for treatment. Radiotherapy is a more precise treatment, because it is based on type, location and stage of the cancer. Boron Neutron Capture Therapy seems to be a very promising radiotherapy in the future. It is a dual approach of cancer therapy which uses a boron-containing compound that preferentially concentrates in tumor sites before being exposed to a neutron beam. The neutrons in the beam interact with the boron in the tumor to cause the boron atom to split into an alpha particle and lithium nucleus, mostly accompanied by the release of a 478 keV γ-ray. Both alpha particle and lithium nucleus have a very short range (about one cellular diameter) and cause significant damage to the cell in which they are contained. Thus, damage is only done to the tumor cell, while largely sparing healthy tissue. Boron Neutron Capture Therapy has been experimentally tested

primarily as an alternative treatment for brain tumours as well as head and neck cancer.

In summary, Boron Neutron Capture Therapy is a highly selective type of radiation therapy that can target the tumor at the cellular level without causing excessive radiation damage to the adjacent normal cells and tissues. Weighted doses up to 70 Gy can be delivered to tumor cells within approximately one hour compared to 6 to 7 weeks for conventional external photon irradiation. However, the effectiveness of Boron Neutron Capture Therapy is dependent upon a relatively homogeneous distribution of boron within the tumor, and this is still one of the key stumbling blocks that has limited its success. There is no doubt that Boron Neutron Capture Therapy is a promising cancer therapy in the near future, but one of most important problems is to solve the monitoring of the treatment effect during neutron irradiation; it is not possible to get a real-time image of the region being treated so far. This project evaluated the use of a Compton camera system to obtain an image of the region being treated by using the characteristic 478 keV γ-rays emitted.

2

Boron Neutron Capture Therapy

In Boron Neutron Capture Therapy (BNCT), the patient is given an intravenous injection of a boron-containing chemical, that preferentially binds to tumour cells. After the injection, the typical boron (^{10}B) concentration in blood and brain is 15 $\frac{\mu g}{g}$ and in a tumor 52.5 $\frac{\mu g}{g}$ (13). When the ^{10}B is accumulated in the tissue, the patient is exposed to a neutron beam. The neutrons produced by the source pass through a neutron moderator, which shapes the neutron energy spectrum suitable for BNCT treatment. Before entering the patient the neutron beam is shaped by a beam collimator. While passing through the tissue of the patient, the neutrons are slowed by collisions and become low energy thermal neutrons. The thermal neutrons are captured by the ^{10}B nuclei, forming a compound nucleus (excited ^{11}B) which then promptly disintegrates to ^{7}Li and an alpha particle. Both the alpha particle and the ^{7}Li have a high energy and range of approximately 5-9 micrometres, which is about the dimension of a cell. Thus the damage occurs only to the tumour cells, in which the reaction products are created, while healthy tissue can be largely spared. The two possible reactions during BNCT are the following,

$$^{10}B + n \rightarrow^{11} B \rightarrow \alpha +^{7} Li + 2.792MeV \text{ (7\% branching fraction)} \quad (2.1)$$

$$^{10}B + n \rightarrow^{11} B \rightarrow \alpha +^{*7} Li + \gamma(478 \text{ keV}) + 2.310MeV \text{ (93\% branching fraction)} \quad (2.2)$$

The characteristic γ-ray is emitted in 93% of the cases, when the excited ^{7}Li deexcites into its ground state as seen in figure 2.1. The 478 keV γ-ray has an attenuation coefficient of around $0.1cm^{-1}$ in soft tissue and can therefore escape from the patient's

body to be detected as a measure of the boron dose. This project evaluated the feasibility of using a Compton camera system to analyse this characteristic 478 keV radiation to obtain an image of the region being treated.

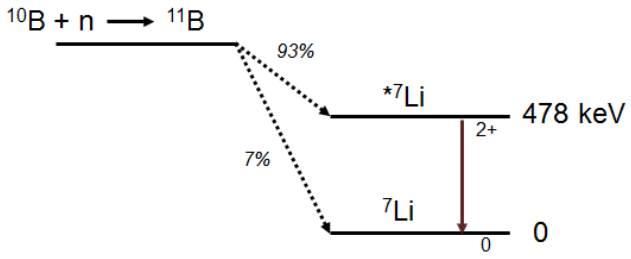

Figure 2.1: Decay of excited ^{11}B - ^{10}B captures a neutron and decays either into the excited state of ^{7}Li (93%) or the ground state of ^{7}Li (7%). A 478 keV γ-ray is emitted when the $^{*7}Li$ de-excites into the ground state

It is possible to provide a neutron source suitable for BNCT from a particle accelerator, which makes it attractive for clinical treatment. Such a facility can be found in Birmingham. BNCT is a complex treatment, which is still in its infancy, but it offers great promise for treating cancer in future.

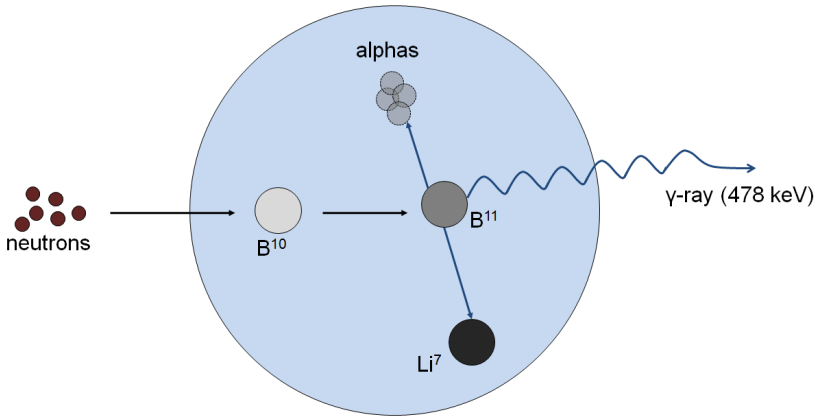

Figure 2.2: Process during BNCT - This is an illustration of the process during BNCT. The ^{10}B captures a neutron and then ^{11}B disintegrates in 93% into an alpha particle excited ^{7}Li nucleus, releasing a 478 keV γ-ray when it de-excites to its ground state

3

Principles of Radiation Detection

3.1 Radiation Interaction Mechanisms

The operation of radiation detectors depends on the way in which radiation interacts with the material of the detector. There are three main interaction processes that play an important role in γ-radiation measurements: Photoelectric absorption (PA), Compton scattering (CS) and pair production (PP). All these processes lead to the partial or complete transfer of the γ-ray energy to electron energy [1]. The different mechanisms are dominant at different energies as shown in figure 3.1.
Each of the mechanisms contributes to the total linear attenuation coefficient μ_t for γ-rays,

$$\mu_t = \mu_{PA} + \mu_{CS} + \mu_{PP} \tag{3.1}$$

The linear attenuation coefficient is used to calculate the intensity I of an incident γ-ray after traveling a distance z through an absorbing material. The intensity can be calculated as follows,

$$I = I_0 e^{-\mu_t z}, \tag{3.2}$$

where I_0 is the initial intensity of the γ-ray before entering the absorbing material.

3.1.1 Photoelectric Absorption

During photoelectric absorption the γ-ray transfers all its energy by producing a energetic photolelectron. Due to energy conservation, the kinetic energy of the photoelectron depends on the binding energy E_b and the energy of the incident γ-ray E_γ,

[1] In pair production energy is also transferred to a positron

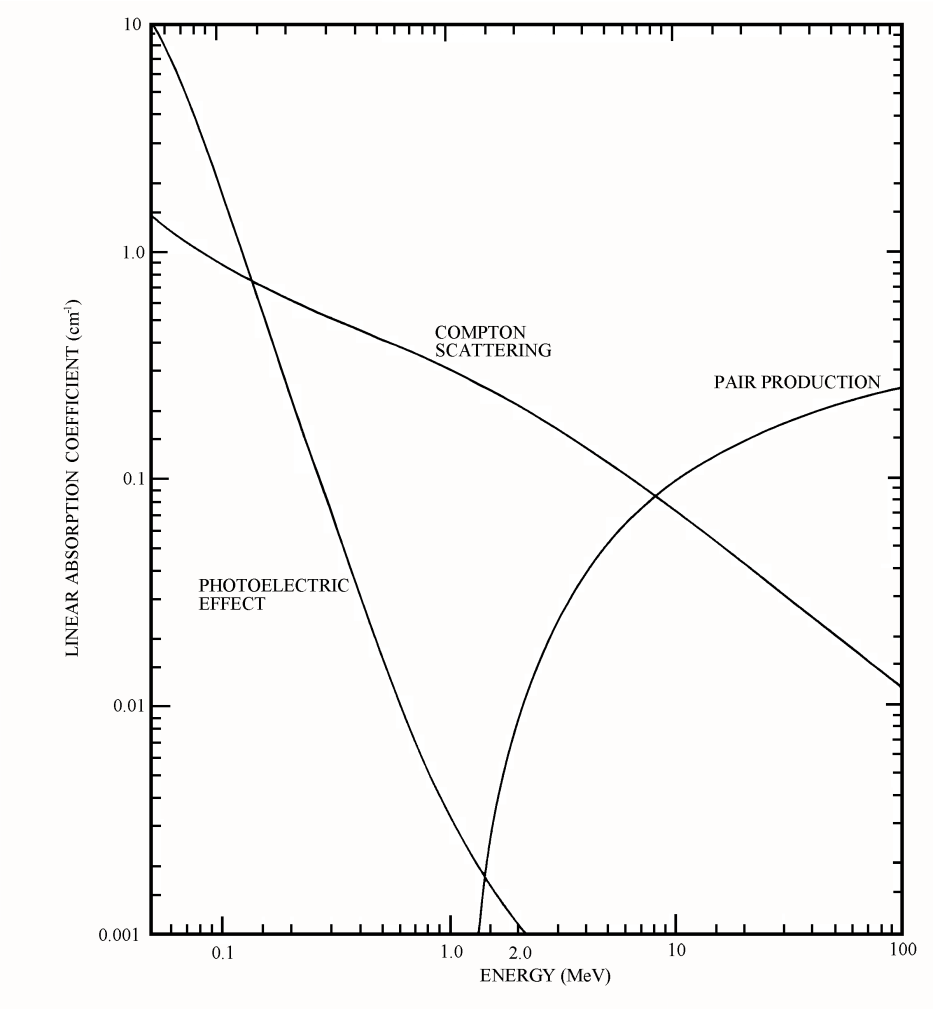

Figure 3.1: Absorption coefficients of the various interaction processes - This plot shows the linear absorption coefficients for photoelectric absorption, Compton scattering and pair production in germanium. At 478 keV γ-ray energy both photoelectric absorption and Compton scattering can occur. Pair production is energetically not possible.

as

$$E_e = E_\gamma - E_b \tag{3.3}$$

In this project, the detector material is germanium with a binding energy of 12 eV for an electron. As a bound electron is removed from the atom's shell, higher state orbital electrons start to rearrange to fill this vacancy. This leads to characteristic x-rays emitted, which may be reabsorbed or may escape the material. The photoelectric absorption primarily dominates at lower energies and is enhanced for absorber materials with a high atomic number Z. The probability of photoelectric absorption per atom can be roughly approximated to

$$\omega_{PA} \approx \frac{Z^n}{E_\gamma^{3.5}}, \tag{3.4}$$

where the exponent n varies between 4 and 5 over the range of γ-rays energies. (2, 4)

3.1.2 Compton Scattering

Compton Scattering takes place between the incident γ-ray photon and a loosely bound electron in the absorbing material. It is predominant over a broad energy range and the investigated Compton camera system is based on the kinematics of Compton scattering. The incoming γ-ray is scattered through an angle θ with respect to its original direction. During this process, the γ-ray transfers some of its energy to the electron, which is assumed to be initially at rest. This electron is referred to as the recoil electron. The energy of the scattered γ-ray depends on the scattering angle, as

$$E_\gamma^{'} = \frac{1}{1 + \frac{E_\gamma}{m_e c^2}(1 - cos\theta)}, \tag{3.5}$$

where $m_e c^2 = 511keV$, $E_\gamma^{'}$ is the energy of the recoil electron and θ is the scattering angle. This relationship is derived from the conservation of energy and momentum. The probability of Compton scattering per atom of the absorber depends on the number of electrons available as potential scattering targets. Thus, it increases linearly with Z. The Klein-Nishina formula predicts the angular distribution of scattered γ-rays for the differential scattering cross section $\frac{d\sigma}{d\Omega}$, as

$$\frac{d\sigma}{d\Omega} = Z r_0^2 \left(\frac{1}{1 + \alpha(1 - cos\theta)^2}\right)\left(\frac{1 + cos^2\theta}{2}\right)\left(1 + \frac{\alpha^2(1 - cos\theta)^2}{(1 + cos^2\theta)[1 + \alpha(1 - cos\theta)]}\right), \tag{3.6}$$

where $\alpha \equiv \frac{h\nu}{m_0 c^2}$ and r_0 is the classical electron radius. Figure 3.2 shows a polar plot of the number of photons Compton scattered into a unit solid angle at the scattering angle θ, and it can be seen that foward scattering dominates at 478 keV.

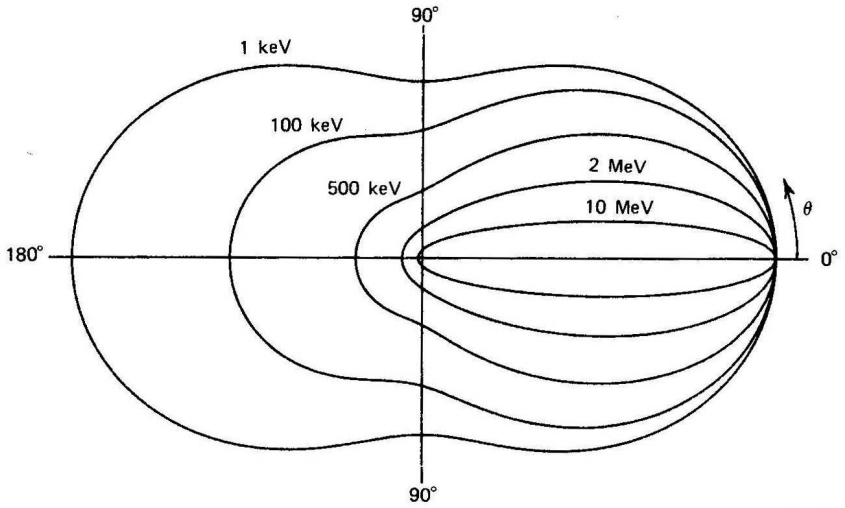

Figure 3.2: Polar Plot of Compton scattered photons - A polar plot of the number of photons Compton scattered into a unit solid angle at the scattering angle θ. The curves are shown for the indicated initial energies. At 478 keV forward scattering dominates.

3.1.3 Pair Production

If the energy of the incoming γ-ray exceeds twice of the rest mass energy of an electron ($2 * 511keV = 1.02MeV$), pair production is energetically possible. Therefore this process predominates at high energies in the many-MeV range. In pair production, the photon disappears and is replaced by an electron-positron pair, with the electron and positron escaping in opposite directions. During the interaction, all the excess energy of the incident γ-ray is transferred to the electron-positron pair in form of kinetic energy shared between the electron and positron. After the interaction has taken place, the positron will subsequently annihilate after slowing down in the absorber material, and two annihilation photons are normally created as secondary products of the interaction. There is no simple expression for the probability of pair production per nucleus, but its magnitude varies approximately as the square of the absorber atomic number. (2). As the energy of the photon emitted during BNCT is only 478 keV, pair production is not energetically possible.

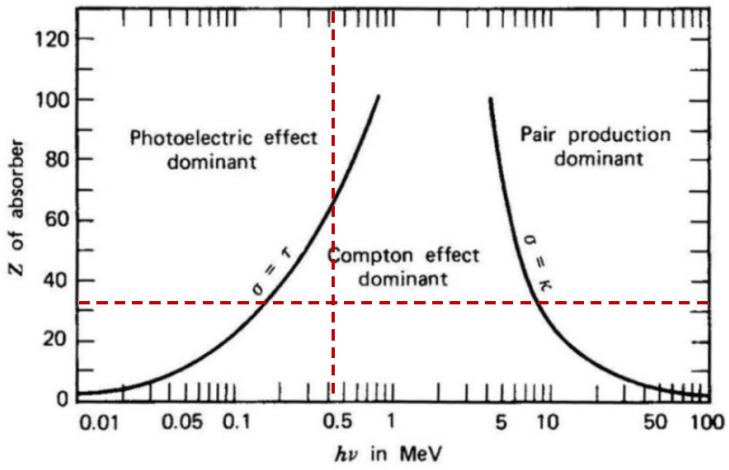

Figure 3.3: Relative importance of main interaction mechanisms - The relative importance of the three main interaction processes. The lines show the values of Z and energy for which the two neighbouring effects are just equal. The red dotted line belongs to Z=32 (germanium) and 478 keV incident energy.

Figure 3.3 shows the domination of the three interaction mechanisms for different absorber materials and γ-ray energies. The black line at the left represents the energy at which photoelectric absorption and Compton scattering are equally probable as a function of the absorber atomic number. The black line at the right represents the energy at which Compton scattering and pair production are equally probable. An illustration of all three interaction mechanisms can be seen in figure 3.4.

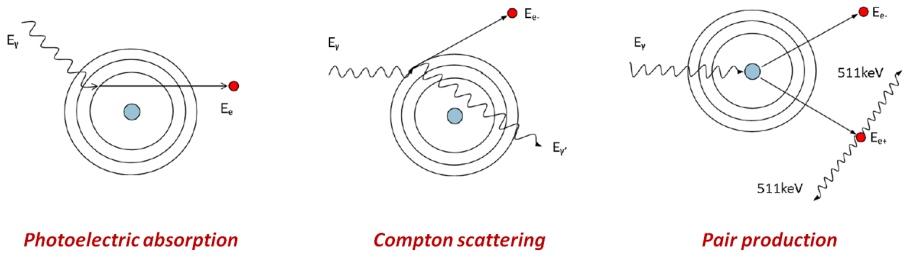

Figure 3.4: The main interaction processes - Illustrations of the three main interaction mechanisms: (a) photoelectric absorption, (b) Compton scattering and (c) pair production

3.2 Electron Interaction Mechanisms

The understanding of electron interaction mechanisms is very beneficial in terms of γ-ray detection methods. The radiation interaction mechanisms described in the previous section are all leading to the creation of electrons (and positrons in pair production). Electrons and positrons are charge carriers and play an important role in radiation detection as charged particles can easily be detected. In contrast to γ-rays, which lose their energy in discrete processes, electrons transfer their energy continuously as they pass through material. The linear stopping power $S = -\left(\frac{dE}{dx}\right)$ is a measure of the average rate of energy loss along the trajectory of a charged particle. The main two types of energy loss for electrons are collisional losses $(\frac{dE}{dx})_c$ and radiative losses $(\frac{dE}{dx})_r$, which sum to give the total linear stopping power as,

$$\left(\frac{dE}{dx}\right)_t = \left(\frac{dE}{dx}\right)_c + \left(\frac{dE}{dx}\right)_r . \tag{3.7}$$

3.2.1 Collisional Energy Loss

The collisional Bethe-Bloch formula describes the specific energy loss $\frac{-dE}{dx}$ of an electron with velocity v incident on an absorber material of number density N and atomic number Z due to electromagnetic collisions,

$$-\left(\frac{dE}{dx}\right)_c \approx \frac{2\pi e^4 NZ}{m_0 v^2}\left(ln\frac{m_0 v^2 E}{2I^2(1-\beta^2)} - g(\beta^2)\right), \tag{3.8}$$

where $g(\beta^2)$ is the density effect correction, a function of the electron velocity and $\beta = \frac{v}{c}$. The parameter I represents the average excitation and ionisation which takes place as the electrons interact with atomic electrons and nuclei through inelastic and elastic scattering. $g(\beta^2) = -ln(2=1)\beta^2$ for high energies and $g(\beta^2) = ln2 + 1$ for low energies.

3.2.2 Radiative Energy Loss

Energy is also lost through Bremsstrahlung (braking radiation). Bremsstrahlung is a radiative loss caused by the deceleration and deflection of electrons in the Coulomb field of the nucleus. Energy is transferred from the electrons to a continuous spectrum of emitted photons which can either be reabsorbed within or escape from the material.

This energy loss is described by the radiative Bethe-Bloch formula which uses the same notation as the equation for the collisional energy loss,

$$-\left(\frac{dE}{dx}\right)_r = \frac{NEZ(Z+1)e^4}{137m_0^2c^4}\left(4ln\frac{2E}{m_0c^2} - \frac{4}{3}\right). \tag{3.9}$$

The loss of energy through radiative terms is much less than via collisional losses and the ratio between them is approximated, as

$$\frac{(\frac{dE}{dx})_c}{(\frac{dE}{dx})_r} \approx \frac{EZ}{700}. \tag{3.10}$$

Thus, radiative losses only become significant if the electron energy is high (many MeV) or if the Z of the absorbing material is high. For low electron energy and absorber material Z radiative losses are minimal. (2, 22)

3.3 Neutron Interaction Mechanisms

As neutrons are neutral, the mechanisms for detecting neutrons in matter are based on indirect methods. The main two types of interactions with matter available are scattering and absorption. The various interactions of neutrons are shown in figure 3.5.

3.3.1 Scattering

Scattering events can be subdivided into elastic and inelastic scattering. In elastic scattering, the total kinetic energy of the neutron and nucleus is unchanged by the interaction. During the interaction, a fraction of the neutron's kinetic energy is transferred to the nucleus. A nucleus of atomic weight A loses on average an energy of $\frac{2EA}{(A+1)^2}$, when colliding with a neutron with kinetic energy E. Elastic scattering is a significant interaction for slow neutrons. Because of the small kinetic energy of slow neutrons, very little energy can be transferred to the nucleus and thus this interaction cannot be used as a basis of neutron detectors. Fast neutrons also undergo scattering, and as the fast neutron can transfer a significant amount of energy in one collision, the secondary radiations in this case are recoil nuclei, which have picked up a detectable amount of energy.

If the energy of the fast neutron is sufficiently high, inelastic scattering with nuclei can take place in which the recoil nucleus is lifted to one of its excited states during

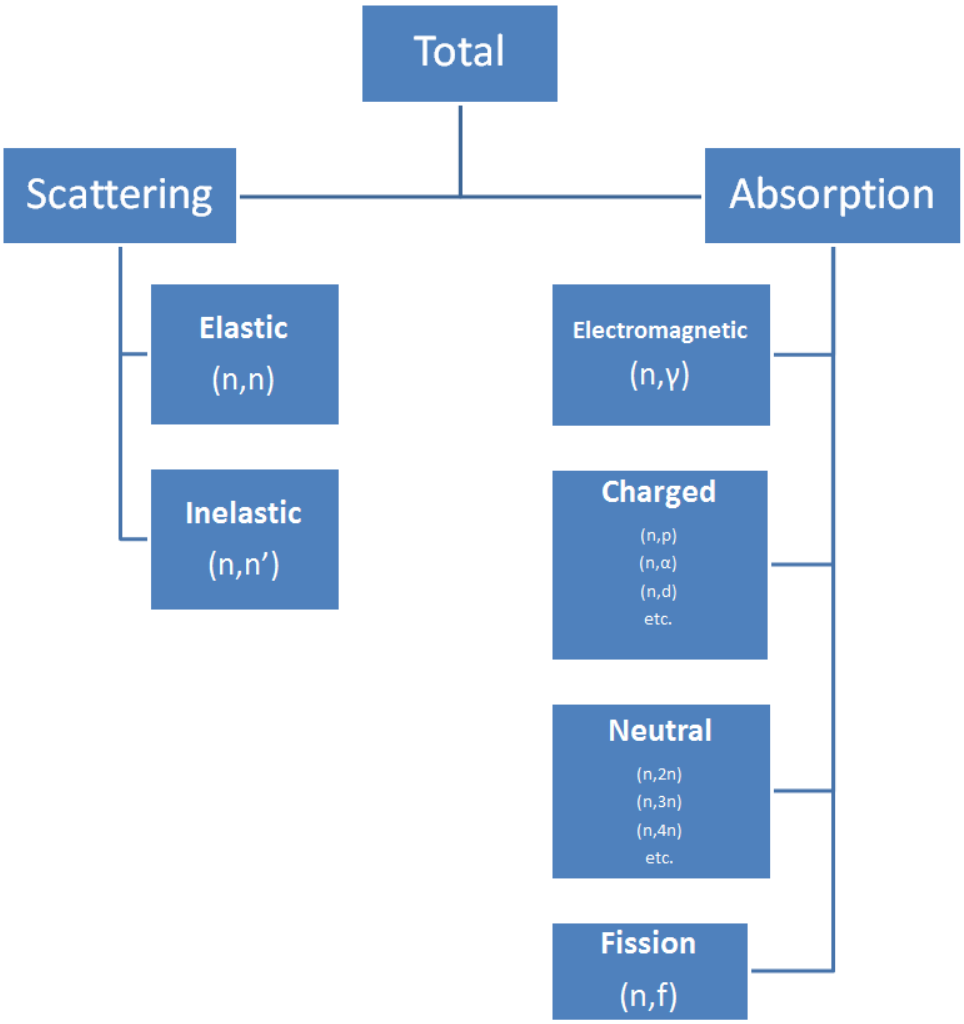

Figure 3.5: Neutron interactions - This shows the various types of neutron interactions. The letters separated by commas show the incoming and outgoing particles.

the collision. The nucleus quickly de-excites, emitting a γ-ray, and the neutron loses a greater fraction of its energy than it would in an equivalent elastic collision. Inelastic scattering and the subsequent secondary γ-rays play and important role in shielding of high-energy neutrons, but are an unwanted complication in the response of most neutron detectors based on elastic scattering.

3.3.2 Absorption

Instead of being scattered by a nucleus, the neutron may also be absorbed or captured. A variety of emissions may follow as seen in figure 3.5. The nucleus may rearrange its internal structure and release one or more γ-rays. Charged particles like protons, deuterons, and alpha particles may also be emitted. There may also be fission events, leading to two or more fission fragments [1] and more neutrons. For slow neutrons the significant interactions include a large set of neutron-induced nuclear reactions. They create secondary radiations of sufficient energy to be detected directly. As the incoming neutron energy is low for slow neutrons, the reactions must have a positive Q-value to be energetically possible. In most materials, the radiative capture reaction, or (n,γ) reaction, is the most probable and plays an important part in the attenuation or shielding of neutrons. Neutron-induced reactions useful for detection are not that important for fast neutrons as the probability of the reactions drops off rapidly as the neutron energy increases.

3.3.3 Moderation

During BNCT fast neutrons have to moderated. The moderation increases the interaction cross section which follows a $\frac{1}{v}$ trend [2]. The expression for elastic scattering shows that in order to reduce the speed of neutrons with the fewest number of elastic collisions, target nuclei with small A should be used. A neutron with 2 MeV of kinetic energy will have 1 MeV left after one collision in water, 0.5 MeV after the second collisions and so on. To achieve thermal energy, about 27 collisions are needed, which is achieved after a few centimetres. From the relation $E = k_B T$ where k_B is Boltzmann's constant, an energy of $\sim 0.025eV$ corresponds to a temperature of 20 degrees. A material with a large moderating power might nevertheless be useless as a

[1] Nuclei of intermediate atomic weight

[2] ^{10}B has a cross section of 3845 barns for thermal neutrons and 2.68 barns for 1 MeV neutrons

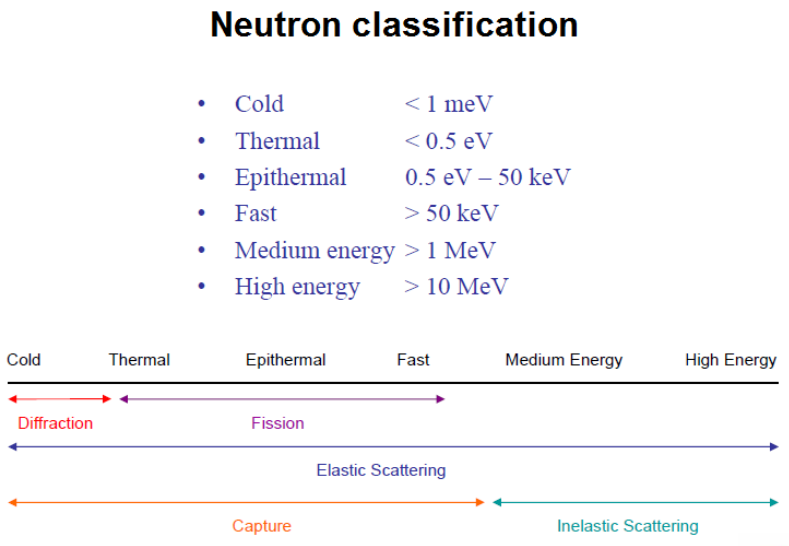

Figure 3.6: Neutron classification - This figure shows which interactions are dominant at different neutron energies.

practical moderator if it has a large absorption cross section. Such a moderator would effectively reduce the speeds of those neutrons that are not absorbed, but the fraction of neutrons that survive may be too small to be used in a practical manner. Ordinary water has a higher moderating power than heavy water because the atomic weight of hydrogen is half that of deuterium. But the hydrogen nucleus (a proton) can absorb a neutron and create deuterium much more readily than a deuterium nucleus can absorb a neutron and create tritium. This difference in absorption cross sections gives heavy water a much more favorable moderating ratio. Polyethylene is commonly selected as a moderator because of its high moderating power and moderating ratio.

Moderator	**Moderating Power** *(1 eV to 100 keV)*	**Moderating Ratio** *(Approximate)*
Water	1.28	58
Heavy Water	0.18	21000
Helium at STP	0.00001	45
Beryllium	0.16	130
Graphite	0.064	200
Polyethylene (CH_2)	3.26	122

Table 3.1: Neutron moderator characteristics - The table shows characteristics of various neutron moderators. The higher the moderating ratio, the quicker high energetic neutrons get moderated.

3.4 Radiation Detectors

The previously explained interaction mechanisms of radiation with matter all lead to creation of secondary charged particles. A net amount of charge is subsequently created inside the detector volume which is then converted into an electrical signal for detection. For this purpose, often solid state detectors are used, which are much denser than comparable gas detectors and have higher stopping powers and higher efficiencies. The main two types of solid state detectors are scintillators and semiconductors. While scintillators offer greater efficiency, semiconductors are preferred for precision experiments as the energy resolution is much better. In this project a semiconductor detector was mainly used for the γ-ray spectroscopy. For the thermal neutron detection a Helium-3 (^3He) tube was used, which will be described later on in this chapter.

3.4.1 Germanium Detector

The germanium detector belongs to the class of the semiconductor detectors, which uses an elemental or compound semiconductor crystal as the detection medium. Semiconductor detectors offer an excellent energy resolution and are widely used when precise energy measurements are required although they are less efficient than common scintillation detectors. Furthermore, they offer a good stability and excellent timing characteristics. The fundamental principles of semiconductors in radiation detection are briefly explained in the following sections.

Band structure of solids In a free atom the electrons can occupy precisely determined energy levels. Each electron in the solid must lie in one of these energy bands, which are separated by gaps or ranges of forbidden energies. Solid materials can be grouped into insulators, semiconductors and conductors according to their electrical properties. Figure 3.7 shows the band structure for electron energies in insulators, intrinsic, n-type and p-type semiconductors. The uppermost occupied energy band is known as the valence band and the next higher-lying band is called the conduction band. The two bands are separated by the band gap, the size of which determines whether the material is a semiconductor or an insulator.

Valence electrons may be liberated with enough energy to overcome the band gap and transfer to the conduction band, resulting in conductivity. The band gap in insula-

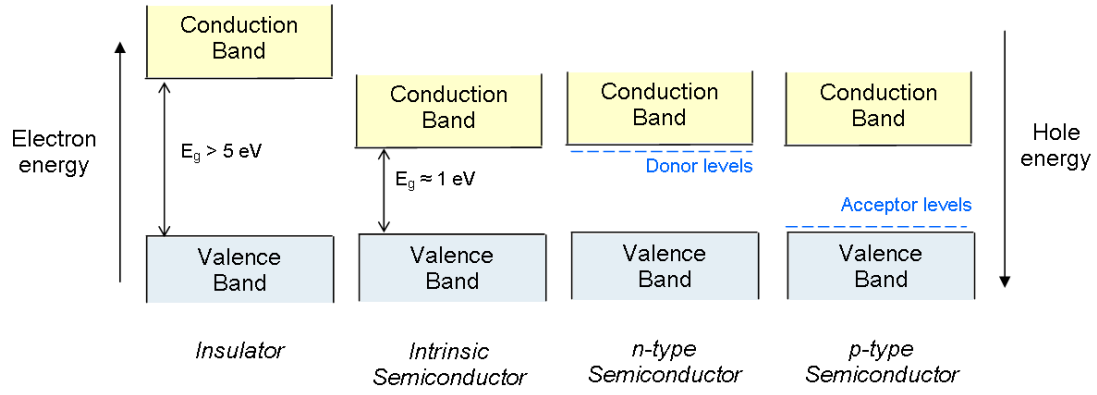

Figure 3.7: Bandstructure of insulator and semiconductor - Schematic diagrams to describe the band structure for electron energies in insulators, intrinsic, n-type and p-type semiconductors

tors is typically larger than 5 eV and therefore conductivity is minimal. Semiconductors have a band gap of approximately 1 eV which can be more easily overcome through thermal excitations.

Charge Carriers When an electron is promoted from the valence band to the conduction band consequently a vacancy is left in the valence band. This vacancy is referred to as hole. The liberated valence electron and hole are called electron-hole pair which are the charge carriers for a semiconductor detector. The probability that an electron will be promoted to the conduction band is strongly influenced by temperature as follows,

$$p(T) \propto T^{\frac{3}{2}} exp\left(-\frac{E_g}{2kT}\right) \tag{3.11}$$

The number of electron-hole pairs produced, N, in the detector depends on the energy of the incident γ-ray, E_γ and the ionisation energy, E_{ion} of the absorbing material

$$N = \frac{E_\gamma}{E_{ion}} \tag{3.12}$$

After electron-hole pairs have been created, they have to be detected. Both charge carriers move in a random ways and eventually recombine. Therefore a strong electric field, to avoid large charge recombination, must be applied, so the charge carriers can migrate to the surface of the detector in opposite directions, parallel to the direction

of the electric field. Therefore most of the semiconductor detectors are operated with sufficiently high electric fields as the drift velocity for the charge carriers saturates. The mobility μ for both electrons and holes can be defined by

$$v_h = \mu_h \epsilon \tag{3.13}$$

$$v_e = \mu_e \epsilon \tag{3.14}$$

where ϵ is the electric field magnitude. For germanium detectors the mobility of the electron and hole are roughly of the same order as shown in table 3.2. The drift velocity increases proportionally as the electric field field strength is increased. The drift velocity typically saturates at the order of $10^7 \frac{cm}{s}$. Therefore the time required to collect the carriers over typical dimensions of 0.1 cm or less will be under 10 ns. This is the reason, why semiconductor detectors are among the fastest-responding of all radiation detector types.

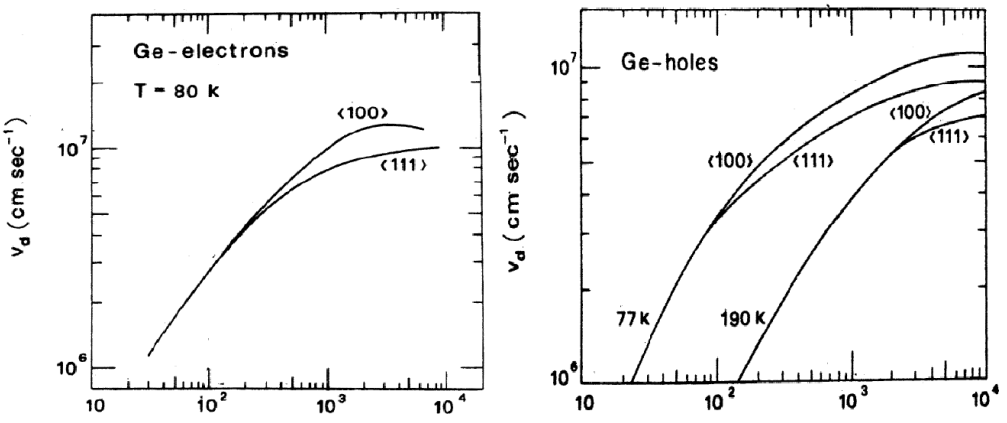

Figure 3.8: Drift velocity in germanium - The drift velocity in germanium as a function of electric field strength applied parallel to the $< 111 >$ and $< 100 >$ crystallographic direction for electrons at 80K and holes at 77K and 190K.

Figure 3.8 shows how the drift velocity varies for electrons and holes in germanium when the electric field is applied parallel to the $< 111 >$ and $< 100 >$ crystallographic axes. The drift velocity of electrons is shown to saturate at an electric field strength of over $10^4 \frac{V}{cm}$, whereas a much higher electric field is required to saturate the drift velocity of holes in germanium. The drift velocity for electrons and holes in the $< 111 >$ direction is shown to saturate at a lower drift velocity than for the $< 100 >$ direction.

Energy resolution The overall energy resolution of a semiconductor detector is given by the combination of four factors

$$\Delta E_{total} = \sqrt{(\Delta E_D)^2 + (\Delta E_X)^2 + (\Delta E_E)^2 + (\Delta E_{Doppler})^2} \tag{3.15}$$

ΔE_D is the inherent statistical fluctuation in the number of charge carriers created and depends on the ionisation energy of the material. The ionisation energy is the energy expended by the primary charged particle to produce one electron-hole pair. For germanium, the ionisation energy is about 3 eV, which is a lot lower than for a scintillation detector (e.g. sodium iodide), which has an ionisation energy of the order 100 eV [1]. This quantity is observed to be independent of both the energy and type of radiation. The number of charge carriers, which produce the electrical signal that can be detected, is directly related to the energy of the incident γ-ray and the ionisation energy; number of charge carriers equals the energy of the incident radiation divided by the ionisation energy. In addition to the mean number of charge carriers, the fluctuation or variance in the number of charge carriers is important. The observed statistical fluctuations in semiconductors are smaller than expected if the formation of the charge carriers were a Poisson process. In the Poisson process it is assumed that every electron-hole pair is totally independent from each other and thus predicts that the variance of the total number of electron-hole pairs is equal to the total number produced. This is not the case as more electron- hole pairs are created when the photoelectron is moving. Therefore the so called Fano factor, F, is introduced to adjust and $\Delta E_D^2 = (2.35)^2 F \epsilon E$, where ϵ is the ionisation energy.

ΔE_X arises from incomplete charge collection, which takes place when the charge carriers recombine before they reach the surface of the detector. Recombined charge carries will not give rise to a signal and therefore lowers the resolution of the detector. The incomplete charge collection can be improved by increasing the detector size, but this is practically limited by cost.

ΔE_E is due to the broadening effects off all the electronic components following the detector like the pre-amplifier, amplifier or multi channel analyser. The last factor $\Delta E_{Doppler}$ is from the Doppler broadening from a moving source.

[1] The chain of events that must take place in converting the incident radiation energy to light and the subsequent generation of an electrical signal involves many inefficient steps

	Silicon	**Germanium**
Atomic number	14	32
Atomic weight	28.09	72.60
Stable isotope mass numbers	28-29-30	70-72-73-74-76
Density (300 K); $\frac{g}{cm^3}$	2.33	5.32
$\frac{Atoms}{cm^3}$	$4.96 * 10^{22}$	$4.41 * 10^{22}$
Dielectric constant (relative to vacuum)	12	16
Forbidden energy gap (300 K); eV	1.115	0.665
Forbidden energy gap (0 K); eV	1.165	0.746
Intrinsic carrier density (300 K); cm^{-3}	$1.5 * 10^{10}$	$2.4 * 10^{13}$
Intrinsic resistivity (300 K); $\omega * cm$	$2.3 * 10^5$	47
Electron mobility (300 K); $\frac{cm^2}{V*s}$	1350	3900
Hole mobility (300 K);$\frac{cm^2}{V*s}$	480	1900
Electron mobility (77 K);$\frac{cm^2}{V*s}$	$2.1 * 10^4$	$3.6 * 10^4$
Hole mobility (77 K); $\frac{cm^2}{V*s}$	$1.1 * 10^4$	$4.2 * 10^4$
Energy per electron-hole pair (300 K); eV	3.62	
Ionisation energy (77 K); eV	3.76	2.96
Fano factor (77 K)	0.085 - 0.16	0.057 - 0.11

Table 3.2: Properties of intrinsic silicon and germanium - The table shows the properties of intrinsic silicon and germanium, which are two common semiconductor materials.

3.4.2 Sodium Iodide Detector

The Sodium Iodide (NaI) detector belongs to the class of the scintillation detectors. It offers a superior efficiency over the semiconductor detectors, but the energy resolution is not very good. It is based on absorbing kinetic energy of incident particles and then radiating away this energy as photons. Photomultiplier tubes (PMT) are used for electronic counting an hence giving a signal. There are mainly two different kinds of scintillation detectors, organic [1] and inorganic. The scintillator used in this experiment was a Sodium Iodide detector doped with Thallium (NaI(Tl)), which belongs to the inorganic alkali-halides class. It yields a very high efficiency and produces intense burst of light compared to other spectroscopic scintillators.

Scintillation process Similarly to the semiconductor charge carrier collection, primary electrons produced by the γ-ray interaction raise secondary electrons to the conduction band leaving holes in the valence band. In some cases the energy given to the electron may not be quite sufficient to raise it to the conduction band. Then the electron and hole could remain electrostatically attracted to each other, as an entity called an exciton. If the electrons are allowed to de-excite by falling back to the valence band they will emit electromagnetic radiation. If this radiation is in, or near optical wavelengths it can be detected by a photomultiplier or other light measuring device to provide the detector signal. Hence the detector material must have a reasonable number of electron-hole pairs produced per unit of γ-ray energy. It would be desirable to a have material with high stopping power for γ-radiation. The spectrometry of the response must be proportional to energy. Scintillators must be transparent to the emitted light and the decay time of the excited states must be short to allow high count rates. The material should be available in optical quality in reasonable amounts at reasonable cost. The refractive index of the material should be near to that of glass (around 1.5) to permit efficient coupling to photomultipliers. Sodium iodide is such a material.

Scintillation activation The band gap of NaI is large and photons emitted by de-excitation of electrons directly from the conduction band would be far outside the visible range. This problem is overcome by using activators. NaI is activated with thallium.

[1] Organic scintillator detectors are mainly used for neutron detection

The introduction of about 10^{-3} mole fraction of the impurity produces defect lattice sites which give rise to extra levels within the forbidden band between the valence and conduction bands. The ground of these activator sites lies just above the valence band and the excited states somewhat below the conduction band. When an electron-hole pair is formed the hole may migrate to a nearby activator site. Electrons in the conduction band and within the exciton band will tend to be captured in by the excited activator states. This means that the photon energy released when these levels de-excite will be lower and the electromagnetic radiation will be of longer wavelength. NaI(Tl) offers an excellent light yield of around $4 * 10^4 \frac{photons}{MeV}$ and has the highest known signal output per unit of radiation absorbed of all presently known scintillators.

3.5 Neutron Detection

In this project, the detection of slow neutrons is required, as BNCT is based upon the capture of thermal neutrons. It is difficult to detect neutrons directly, as they carry no charge. Therefore neutrons are generally detected through nuclear reactions that result in prompt energetic charged particles such as protons, alpha particles, and so on. These charged secondary particles can be easily collected. The cross section gives the probability of a particular event occurring between a neutron a nucleus. The cross section for neutron interactions in most materials is a strong function of neutron energy. ^{10}B has an cross section of 3845 barns for thermal neutrons, but only 2.68 barns for 1 MeV neutrons. ^3He has an cross section of 5337 barns for thermal neutrons and only 2.87 for 1 MeV neutrons. Therefore different methods have been developed to detect neutrons.

3.5.1 Nuclear Reactions

The cross section for the reaction must be as large as possible so that an efficient detector can be built with small dimensions. The Q-value is an important quantity in the nuclear reactions as it determines the energy liberated in the reaction following neutron capture. All the conversion reactions are sufficiently exothermic, so that the kinetic energy of the reaction products is determined solely by the Q-value of the reaction as the energy of the incoming thermal neutron is negligible. Due to the conservation of energy and momentum, the reaction products escape in opposite directions. Thus,

to capture the full kinetic energy of these products, the detector must be designed with an active volume that is large enough to fully stop the particles. If the detection medium is a solid, this requirement is easily achieved, because the range of any of the reaction products does not exceed a few tenths of a millimeter in any solid material. If the detector material is a gas, like ^3H used during this project, however, ranges of the reaction products (typically several centimeters) can be significant compared with detector dimensions and some may not deposit all their energy. This leads to the so called wall effect that will be elaborated further in the next section.

The $^{10}B(n,\alpha)$ Reaction One reaction for the conversion of slow neutrons into directly detectable particles is the $^{10}B(n,\alpha)$ reaction. The reaction may be written

$$^{10}B + n \rightarrow^7 Li + 2.792MeV(\text{ground state}) \tag{3.16}$$

or

$$^{10}B + n \rightarrow^7 Li + 2.310MeV(\text{excited state}) \tag{3.17}$$

When thermal neutrons with an energy of 0.025 eV are used to induce the reaction, about 93% of all reactions lead to the excited state and only 7% directly to the the ground state. In either case, the Q-value of the reaction is very large (2.310 or 2.792 MeV) compared with the incoming energy of the slow neutron, so that the energy imparted to the reaction products is essentially just the Q-value itself. Because the incoming linear momentum is very small, the reaction products must be emitted in exactly opposite directions, and the energy of the reaction will always be shared in the same manner between them. Individual energies of the alpha particle and lithium nucleus can be calculated by conservation of energy and momentum,

$$E_{Li} + E_\alpha = Q = 2.31MeV \tag{3.18}$$

$$m_{Li}v_{Li} = m_\alpha v_\alpha \tag{3.19}$$

$$\sqrt{2 * m_{Li}E_{Li}} = \sqrt{2 * m_\alpha E_\alpha} \tag{3.20}$$

Solving these equations simultaneously gives

$$E_{Li} = 0.84MeV \tag{3.21}$$

and

$$E_{\alpha} = 1.47MeV \tag{3.22}$$

where the calculation has been carried out for the case of populating the excited state of ^7Li. A similar calculation would yield larger values by 21% for reactions leading to the ground state.

The $^6Li(n,\alpha)$ reaction Another reaction for the detection of slow neutrons is the (n,α) reaction in ^6Li. Here the reaction proceeds only to the ground state of the product and is written as

$$^6Li + n \rightarrow^3 He + \alpha + 4.78MeV(\text{Q-value}) \tag{3.23}$$

The calculation of the reaction product energies for negligible incoming neutron energy yields the following:

$$E_{^3H} = 2.73MeV \tag{3.24}$$

$$E_{\alpha} = 2.05MeV \tag{3.25}$$

The alpha particle and triton produced in the reaction must be oppositely directed when the incoming neutron energy is low.

The $^3He(n,p)$ reaction The gas ^3He is also widely used as a detection medium for neutrons through the reaction

$$^3He + n \rightarrow^3 H +^1 H + 764keV(\text{Q-value}) \tag{3.26}$$

For reactions induced by slow neutrons, the Q-value of 764 keV leads to oppositely directed reaction products with energies

$$E_{^1H} = 573keV \tag{3.27}$$

and

$$E_{^3H} = 191keV \tag{3.28}$$

The thermal cross section for this reaction is 5330 barns, significantly higher that that for the boron reaction.

3.5.2 Helium-3 Detector

In this project, a Helium-3 (^3He) detector was used for the thermal neutron detection, which is based on the $^3He(n,p)$ reaction. As most of the proportional counters, the ^3He tube is constructed using a cylindrical outer cathode and central wire anode. The detector used in the neutron lab is manufactured out of stainless steel. This is superior to aluminum as aluminum normally shows a small amount of low-level alpha activity.

An important consideration in many applications is the ability to discriminate against γ-rays, which often are found together with the neutron neutron flux to be measured. γ-rays interact primarily in the wall of the counter and create secondary electrons that may produce ionization in the gas.
In a large detector, each thermal neutron reaction would deposit 764 keV in the form of kinetic energy of the triton and proton reaction products. Because the range of these reaction products is not always small compared with the dimensions of the proportional tube, however, wall effect have to be taken into account.

An advantage of the Helium-3 detector is that its neutron cross section is almost 40% higher than the cross section of ^{10}B. It is also a better proportional gas than BF_3. But Helium-3 is expensive as its natural abundance is very low; Helium-3 0.000138%, Helium-4 99.999862%. Helium is poor at stopping neutrons, so Ar or Kr (at 5-20% levels) are sometimes added to increase the stopping power.

Wall effect Figure 3.9 shows the expected spectrum of a ^3He-tube in which the wall effects are significant. In a detector with very large dimensions, nearly all the reactions would occur sufficiently far from the walls of the detector to deposit the full energy of the products within the proportional gas. In this case all of the energy of the reaction would be deposited in the detector. However, for a smaller detector, the size of the tube is no longer large compared to the range of the reaction products. In this scenario, some events no longer deposit the full reaction energy in the gas. If either of the particles, proton or triton, strikes the chamber wall, a smaller pulse is produced. This effect of this type of process is known as the wall effect in the gas counters. In figure 3.9 the continuum to the left of the peaks correspond to partial energy deposition in the gas of the tube. The two steps or discontinuities in the continuum are an interesting feature and can be explained through the following argument. Because the incoming neutron has negligible momentum, the two reactions products must be oppositely directed. If

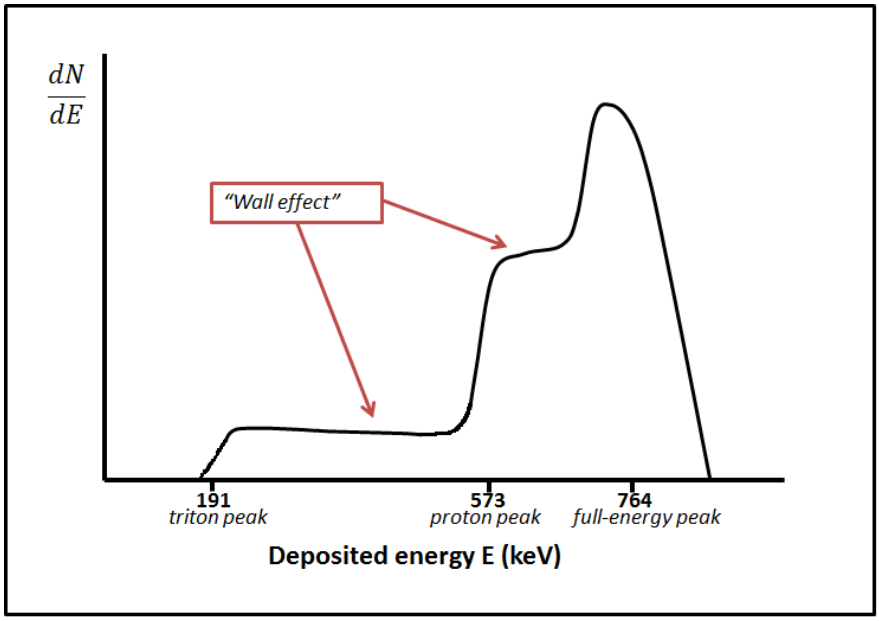

Figure 3.9: Expected pulse height spectrum from a ^3He-tube - This shows the expected pulse height spectrum from a ^3He-tube in which the wall effect is significant

the proton strikes the wall, the triton is therefore directed away from the wall and likely to deposit its full energy within the gas. Conversely, if the triton strikes a wall, the entire energy of the proton from the same reaction is fully absorbed. Thus it is expected to see wall losses for only one of the reaction products at a time. Nevertheless, the reaction could also occur at a distance from the wall that might be anywhere between zero and the full proton range. The amount of energy deposited in the gas can then vary from E_{triton} to $E_{triton} + E_{proton}$. Because all locations of the reactions are more or less equally probable, the distribution of deposited energy will be approximately uniform between these two extremes. Parallel arguments can be made, to show that the energy deposited in the gas will vary from E_{proton} to $E_{proton} + E_{triton.}$. Therefore figure 3.9 shows the two wall effect events and the location of the full-energy peak, that results, when both products are fully absorbed in the gas. The wall effect continuum extends from $E_{triton} = 191keV$ up to the full-energy peak $E_{triton} + E_{proton} = 764keV$. (2)

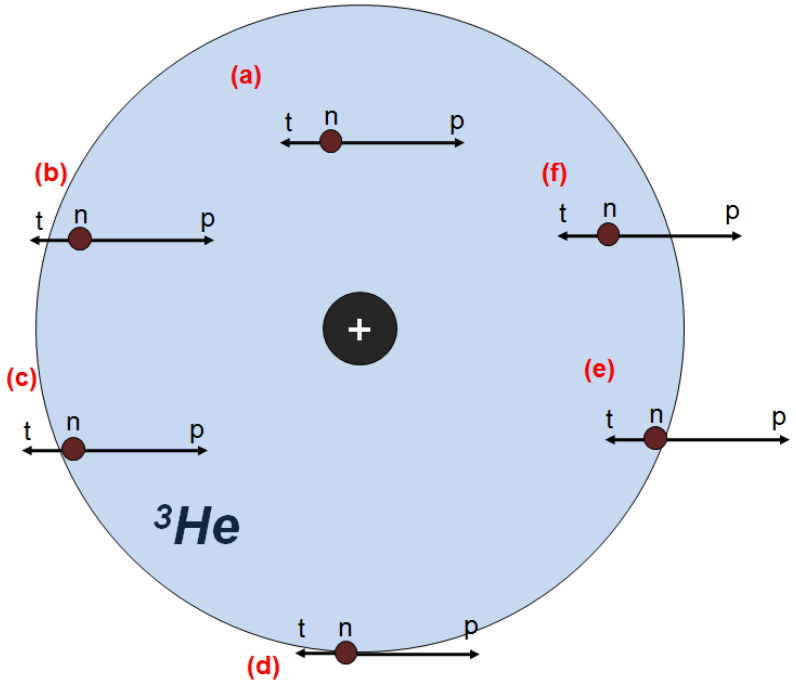

Figure 3.10: Walleffect in ^3He-tube - The decay products, proton and triton, ionize and the created electrons are collected at the positively charged anode (wire). This shows the possible energy depositions in a ^3He-tube leading to the walleffect continuum.: (a) both proton and triton deposit the full energy, 764 keV (b) triton only deposits a part of its energy while proton deposits full energy (c) only proton deposits its energy, 573 keV (d) both proton and triton escape the detector and no energy is deposited (e) only triton deposits its energy, 191 keV (f) proton only deposits part of its energy while triton deposits full energy.

4

Compton Camera

The Compton Camera is a very promising tool in medical imaging. Compton cameras are used for source imaging based on the Compton scattering kinematics. The system consists of at least two position and energy sensitive detectors; scatter detector and absorber detector. The feasibility of utilising a Compton camera in medical applications has been shown through Monte-Carlo simulations and prototype systems, but the full potential has not yet been met as these early investigations were hindered by practical limitations (4). A Compton Camera requires

- Detectors with very low noise properties
- Readout electronics with high data-rate processing capabilities
- Computing resources capable of processing the data through intensive image reconstruction algorithms

4.1 Operation Principle

In an ideal system, the γ-rays emitted from a source placed in front of the scatter detector will Compton scatter from an electron in the first detector, depositing a fraction of its energy before getting fully absorbed in the analyser detector [1]. The sum of the two energies detected in the detector equals the energy of the incident γ-ray and the positions, where the γ-ray interacts with the detector are known. The Compton scattering

[1] The incident γ-rays can also undergo multiple interactions in the detectors. These events are more difficult to process.

formula is used to calculate the scattering angle between the incident and the scattered photon. This scattering angle is then used to form a cone with apex angle 2θ as shown in figure 4.1. Although the scattering angle is known, the direction in which the γ-ray travels is not. The possible origins of the incident γ-ray lie somewhere on the perimeter of this cone. Images are created by overlapping cones from many interactions.

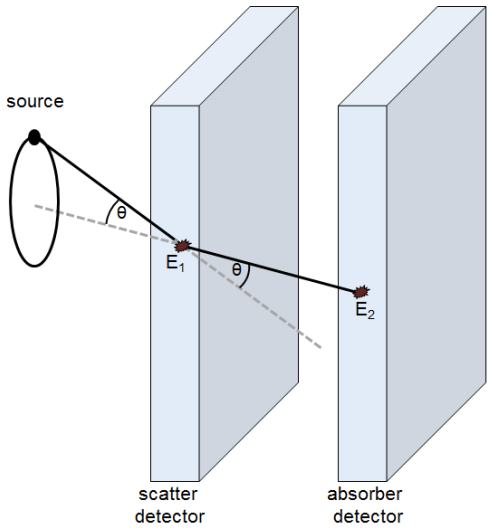

Figure 4.1: Dual layer Compton camera - This is an illustration of a dual layer Compton Camera. It consist of a scatter detector and an absorber detector. The cone is reconstructed using Compton kinematics

4.2 Image Quality

The generation of high quality images by the Compton camera system is required when used in medicine. There are three main factors influencing the image quality; energy resolution, position resolution and Doppler broadening. The overall angular uncertainty and therefore uncertainty in the image reconstructed is given by,

$$\Delta\theta_{total} = \sqrt{(\Delta\theta_{Doppler})^2 + (\Delta\theta_{Energy})^2 + (\Delta\theta_{Position})^2} \tag{4.1}$$

where $\Delta\theta_{Doppler}$ is due to Doppler Broadening in the scatter detector material and defines the ultimate performance of the camera, $\Delta\theta_{Energy}$ is due to the energy resolution in the detectors and $\Delta\theta_{Position}$ arises from the position resolution. These contributions can be briefly explained as follows.

4.2.1 Position Resolution

Position sensitivity of the interactions is responsible for determining the cone axis, about which the cone angle is situated. It is estimated by using the actual hit positions from the strip/pixel size of the detectors. The segmentation of the detectors used in this experiment allows the interaction position to be determined within a 5 mm x 5 mm pixel. In another experiment it has been shown that the position sensitivity through pulse shape analysis can be reduced to a 1 mm x 1 mm x 1 mm voxel, thereby increasing the accuracy of the cone axis position (5).

4.2.2 Energy Resolution

The energy deposited in the scatter detector from the photon is used to calculate the angle of the reconstructed cones axis. A poor energy resolution gives a larger uncertainty in the angle of the cone, leading to a larger uncertainty in the position of the cone base. Germanium has a much better energy resolution than Sodium Iodide for example and is despite its lower efficiency the better detector material for this purpose.

4.2.3 Doppler Broadening

The other contribution to the overall image resolution is Doppler broadening. The reconstruction is performed on the basis of Compton kinematics, in which the target electrons are assumed to be free and at rest. In a real detector, however, target electrons are bound to their atomic nuclei with non-zero orbital momentum. Thus, the uncertainties of the binding energy and the orbital momentum lead to a degradation of the angular resolution in Compton cameras. The effect of the Doppler broadening becomes smaller as the incident energy becomes higher, because the binding energy and momentum of electrons in material are relatively small for γ-rays at higher energies (21). The Z-dependence of Doppler broadening has been investigated and it was shown that the energy spread for germanium is larger than that of the silicon. The germanium crystal with the higher atomic number has potentially more pre-collision momentum states available for their atomic electrons than the silicon crystal with lower Z does. (3)

5

GAMOS simulations

5.1 Objective

To investigate the feasibility of using a Compton camera system during BNCT, GAMOS simulations with the 478 keV γ-ray were performed. GEANT4 is an object-oriented toolkit that implements extensive Monte-Carlo techniques in the C++ programming language to simulate in detail the interaction of particles in matter. GAMOS is a GEANT4-based framework primarily developed for the use in medical physics. Simulations were run to investigate various features like the position resolution and the minimum number of cones [1] for a good image reconstruction. Subsequently, simulations were performed to optimise the Compton camera system. The GAMOS simulation have previously been validated by Dr Laura Harkness for an γ-ray energy of 122 keV. (4)

5.2 Implementations and Detector Geometry

GAMOS requires an accurate input of the experimental setup. In this project, the Compton camera setup consisted of two germanium detectors. The detectors and an isotropic source emitting 478 keV γ-rays were simulated. As at 478 keV forward Compton scattering dominates, the detectors were positioned behind each other. Figure 5.1 shows a snapshot of the two detectors of the Compton camera placed inside the "world". The world represents the space, in which the particles are tracked [2].

[1] and the number of γ-rays required for this number of cones

[2] The bigger the world, the longer it takes to compute the simulation.

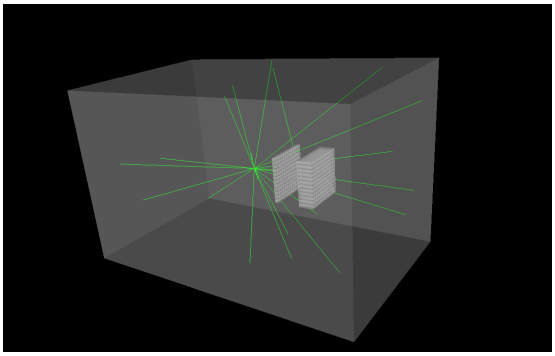

Figure 5.1: Snapshot of Compton camera in GAMOS - Snapshot of the two detectors of the Compton camera placed inside the "World". The green lines represent the γ-rays emitted from a point source in front of the Compton camera

Two main files, input and geometry, are required to run the simulation. The input file (Appendix A) includes various information about the simulations, e.g. it defines what physics packages [1] are used and what histograms are produced. Furthermore, the input file defines the energy and gate for the photopeak of interest and includes event classifiers to get information on the sensitivities. It also contains the information about the resolutions [2] in both detectors and the measuring time of both detectors. The geometry file (Appendix A) contains information about the size and the material of the detectors. It also defines the distances between the source and the scatter detector and the separation between the two detectors.

5.3 Data Generation and Processing

Data were generated using GEANT4 to produce a chosen number of isotropic primary [3] γ-rays for the photopeak energy of 478 keV. A catalogue of information regarding each gamma ray interaction was extracted from the simulation, such as energy deposited, time of interaction and position of interaction using standard GEANT4 functions to

[1] GEANT4 is a versatile package which provides the user the choice of physical processes to be attributed to the particles which have been defined.

[2] Infinitely good resolution is chosen in most of the cases to give the best possible reconstruction

[3] A primary particle in GEANT4 is defined as a particle which arises through the initial generation of events, whereas secondary particles are produced through the interactions of the primary particles, for example an electron becomes a secondary particle in the Compton scattering interaction of a primary γ ray.

write the information to an output file.
Each primaryγ-ray was given a unique ID number, so it is possible to independently track each gamma-ray. In addition, each gamma-ray interaction was assigned an interaction number i corresponding to the i^{th} interaction of that particular gamma ray. An algorithm written for the ROOT [1] data analysis framework was used to analyse the number of full energy deposits in the simulation.

Event Classification The incident γ-rays on the Compton camera system can undergo multiple interactions in the detectors. This can be seen in figure 5.2 By default,

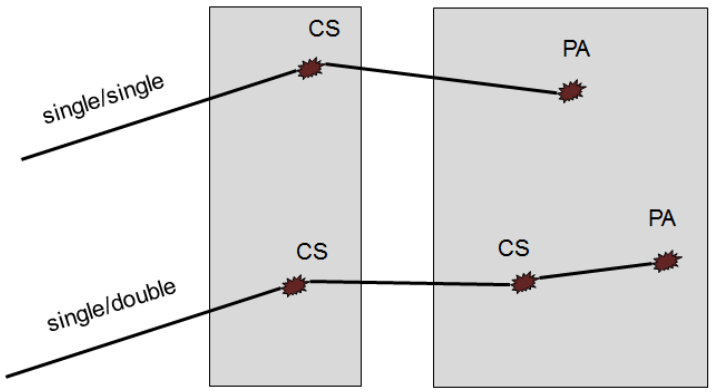

Figure 5.2: Event classification in GAMOS - This is an illustration of how GAMOS classifies events with multiple interactions. A single/single event represents a γ-ray that Compton scatters in the first detector before being absorbed in the second detector.

GAMOS only uses so called single/single interactions when generating the output files. A single/single event represents the case, in which a γ-ray scatters once in the first detector before being fully absorbed in the second detector without further scattering. Single/single events are easy to process and can easily be reconstructed. This is of course not the only possible event an incident γ-ray can undergo. A single/double event describes an γ-ray, that is being Compton scattered in the first detector, undergoing another scattering in the second detector before being fully absorbed.
It has to be stated, that the event classification in GAMOS is simplified. The detectors

[1] An object oriented framework for large scale data analysis.

of the Compton camera are segmented into voxels [1] $[mm^3]$. In GAMOS a single interaction states that the energy is deposited in only one voxel, but it does not specify how many interaction have actually taken place. Therefore a γ-ray can theoretically interact three times [2] in the same voxel, but still be recorded as one interaction in GAMOS. Furthermore, GAMOS always considered the interaction to take place in the centre of one voxel. This gives rise to an uncertainty in position resolution, when reconstructing the cone.

5.4 Image Reconstruction

Potentially each γ-ray can be used to reconstruct a cone and the source location is identified as the area with the greatest overlap of the Compton cones. The images are

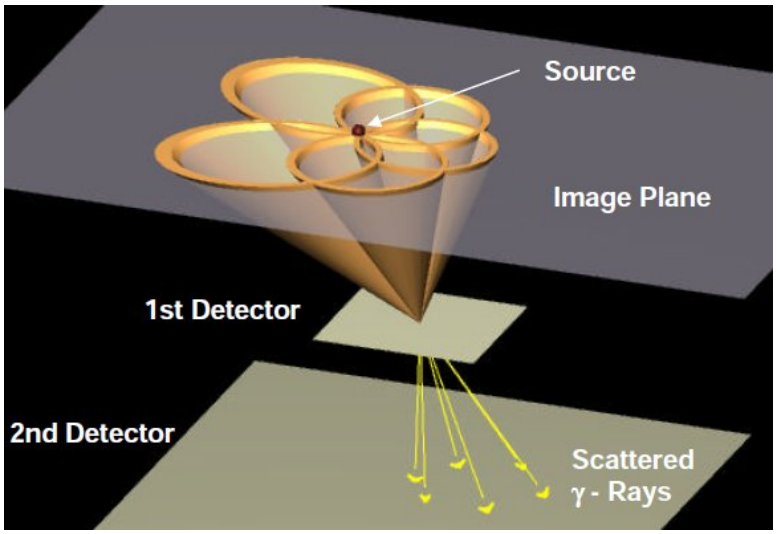

Figure 5.3: Image reconstruction - Illustration of the image reconstruction by overlapping cones

created by overlapping cones, using an imaging code, Compton 3.5, written by Dr Dan Judson. The code is fed with the GAMOS output file to create ROOT files to produce plots of the source. The code is written in C++ and allows to input the required data to call the imaging code before producing the intensity plots. The code takes a Compton camera data set from the GAMOS simulation to produce the intensity plots

[1] A voxel is a volumetric pixel

[2] The three interactions are simulated by GEANT4

or Compton images. The program works by calculating the size and position of the 2D conics that are produced, when a cone is sliced at a given angle and z-distance [1]. These conics are then projected onto a 2D imaging plane to produce 2D images. The program produces a 2D matrix (slice) of intensity vs position in the xy-plane along with the 1D intensity profiles, in the x- and y-axis of this slice through the point of maximum intensity. These 1D profiles are fitted using a custom function to determine the FWHM, which is the position resolution of the distribution. The FWHM is then plotted for a number of different z distances to get an indication of the source location in depth. For the source to be reconstructed, a number of data have to be entered in Compton 3.5. The input file has to be entered and the correct offset chosen in order to produce a good image. It has to be specified whether 1 or 2 peaks should be fitted and how many channels should be used for the reconstruction. The code produces slice images with Lorentzian fits to the x and y slices and also produces chi-squared and FWHM values, that are displayed. The spectra and fits are written to a ROOT file for each slice that is imaged.
It is important to note that the imaging code does not draw a continuous line along the perimeter of the cone base. Instead it draws one voxel per degree (360 in total). Therefore an overlap is only recorded if two voxels of two cones intersect with each other.

Images and Plots The Compton imaging code will read through the data file and determine the total number of events and the number of events which pass the entered energy and angle gates. Each of the accepted events will then be reconstructed into a Compton image for each specified z slice. For each slice a 2D plot of intensity in the xy-plane is produced, along with a slice through this in both the x- and y-planes. These x and y planes are then fitted assuming a Lorentzian peak on a quadratic background. The FWHM and Chi-squared/DOF [2] for each fit are displayed. For each z value, a ROOT file is produced which contains the 2D and 1D intensity plots along with the fits.

[1] The z-distance equals the distance of the source to the detector
[2] DOF = degree of freedom

5.5 Results

5.5.1 Position Resolution

The position resolution of a point source, which is located a distance away from the detector system, has been investigated. The simulation was setup with a total of 70,000,000 beams to give a sufficient number of γ-rays and cones for the reconstruction of the source. Figure 5.4 shows the geometry of the simulation. The two detectors have the same width and length, 60 mm x 60 mm, but vary in thickness. The scatter and absorber thickness is 5 mm and 20 mm, respectively. This represents a realistic setup, as the scatterer and analyser detector have to be placed in vacuum chambers. Therefore the minimum separation between the two detectors is 30 mm.

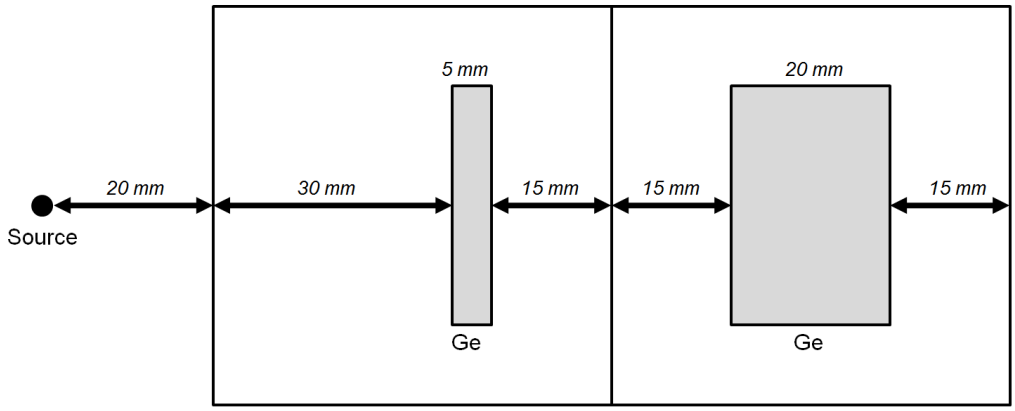

Figure 5.4: Detector setup in GAMOS - The detector setup of the GAMOS simulation. The detectors are separated by 30 mm. The black boxes represent the vacuum boxes, in which the detectors would be placed in an experiment.

The simulations were run for 25 different points on a 10x10cm grid. The setup can be seen in figure 5.5.The isotropically 478kev gamma-ray emitting source was placed successively at each point of the grid [1]. It can be seen that always around 86% of the cones given by GAMOS are used for the image reconstruction. The loss of the 14%, can be explained with the "drawing" of the cone as explained in the previous section.

In order to investigate how the number of cones used for the image reconstruction varies at different distances away from the detector, the output file was fed into a

[1]The detectors are stationary, while the source is moved relatively to the detectors

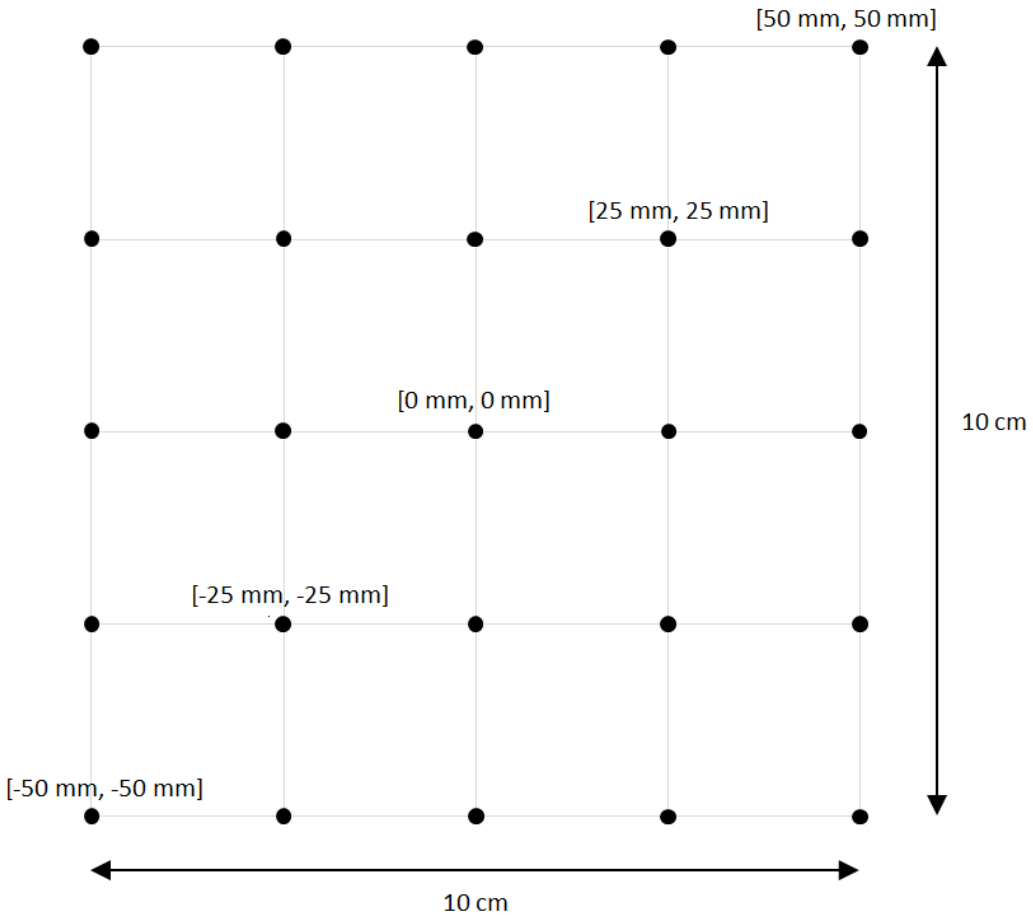

Figure 5.5: Source positions in GAMOS - This is the investigated 10 cm x 10 cm grid in GAMOS with each dot representing a position of the point source.

MATLAB code, which produces a colour intensity plot.

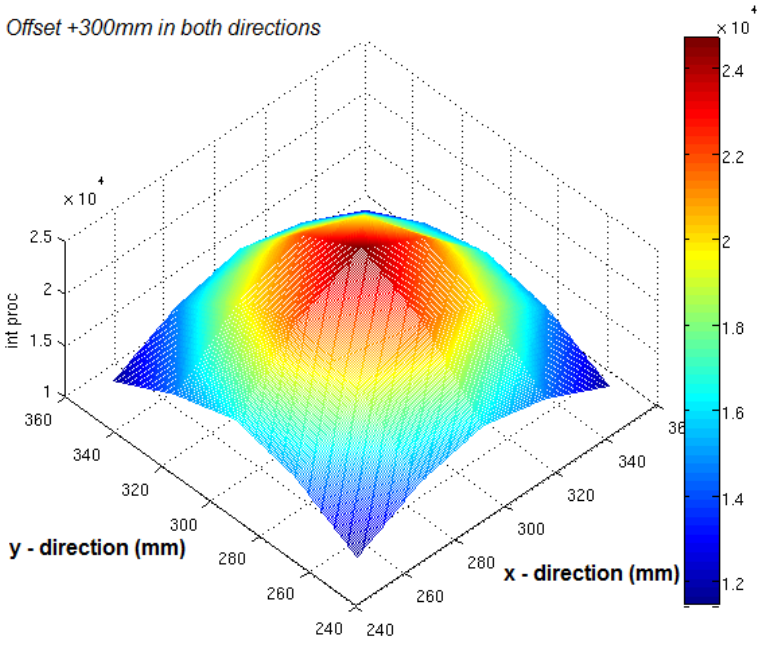

Figure 5.6: Number of events at different source positions (3D) - This colour intensity chart shows the number of cones used tor the image reconstruction against the x-position and y-position (in mm) of the source in 3D. An offset of 300 mm was added in both directions.

As figure 5.6 and 5.7 illustrate, the number of cones decreases significantly as the source moves away from the center of the detector. Figure 5.8 shows how the reconstructed position of the source differs from the actual position of the source [1].The position of the sources drifts towards the inside of the grid and the further away the point is from the center, the greater is the difference between the reconstructed and actual location. This is a systematic error that must be taken into account for a correct image reconstruction. Figure 5.9 shows a typical source image and its projection in x-direction [2].

[1]The actual position refers to the position as it is defined in GAMOS
[2]The projection is similar in y-direction

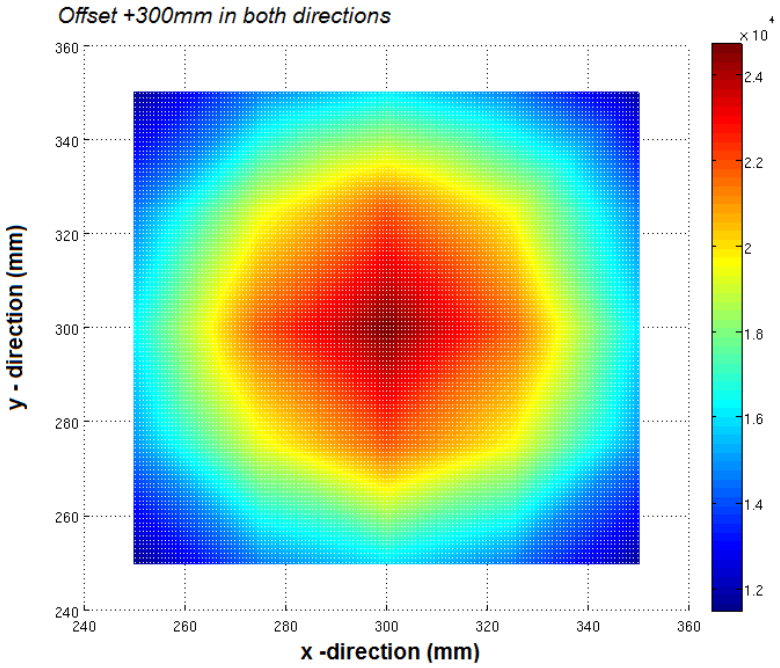

Figure 5.7: Number of events at different source positions (2D) - This colour intensity chart shows the number of cones used tor the image reconstruction against the x-position and y-position (in mm) of the source in 2D. An offset of 300 mm was added in both directions.

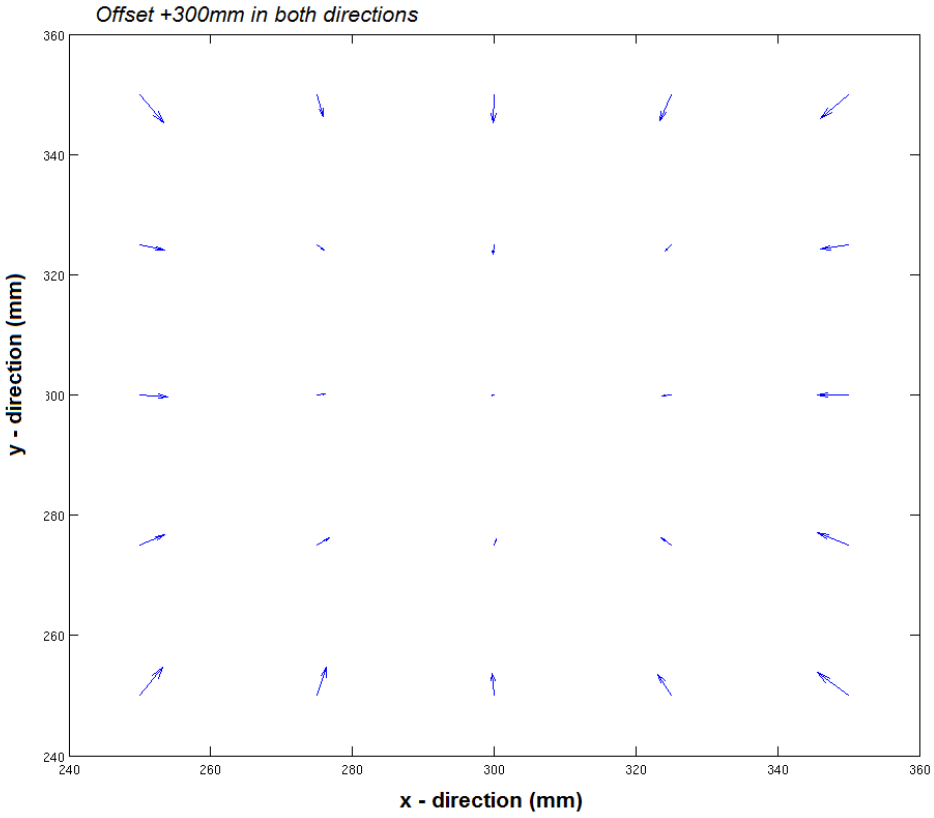

Figure 5.8: Quiver plot - The quiverplot shows the difference between the measured and actual positions of the point source represented with vectors.

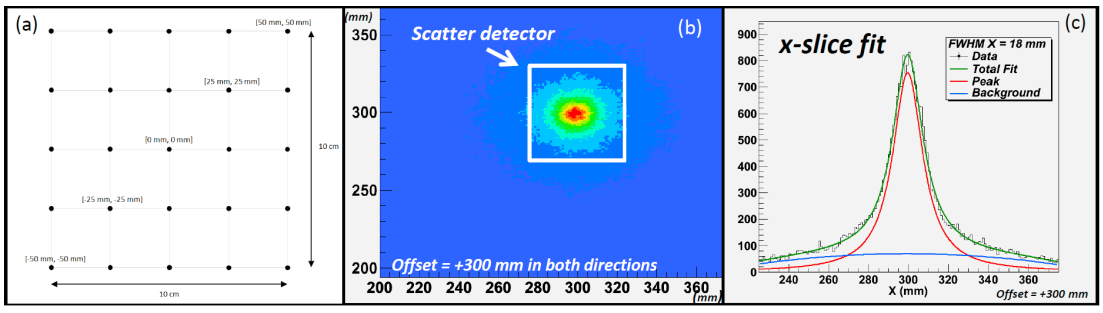

Figure 5.9: Typical image reconstruction of point source - (a) shows the 10cm x 10cm grid being investigated, (b) shows the typical reconstruction of a source by overlapping cones at the [0mm,0mm] and (c) shows the fit of this image. A Lorentzian peak is fitted on a quadratic background.

5.5.2 Energy Deposition in the Detectors

The energy deposition in the scatter and absorber detector was investigated. Only the fully absorbed events [1] were considered, so the full 478 keV has to be deposited in both detectors. To visualise the amount of energy in the scatterer and absorber detector respectively, a script in MATLAB was written to plot a matrix showing the energy absorbed in the scatterer against the energy absorbed in the analyser detector. Three different positions, (0,0) [2] , (25,25) and (50,50), have been plotted.

On average 173 keV is deposited in the scatter detector, and the remaining 305 keV is absorbed in the second detector. By zooming into the region of interest, it can be seen that as the source moves away from the center of the detector, the region of interest shifts to the left. This means, that more energy is lost during the scattering. This can be explained with the solid angle effect as a larger scattering angle leads to more energy loss in the first detector.

5.5.3 Peak to Total

The number of counts in the peak of the sum energy of all coincident events was divided by the total number of events. For the (0,0) position with 70,000,000 γ-rays, the peak to total was found to be 0.326. The corresponding peak to total for the (25,25) and (50,50) position were found to be 0.335 and 0.374 respectively. The highest peak to total at the (50,50) position is expected, as the γ-rays lose more energy due to the larger scattering angle in the first detector and therefore have a higher chance of being absorbed in the absorber detector. If the scattering angle is small, the γ-rays are more energetic and might travel through the second detector or undergo multiple interactions.

[1] A event is considered to be fully absorbed within ± 1 keV of the photopeak energy

[2] (0,0) represents source position at x = 0 mm and y = 0 mm.

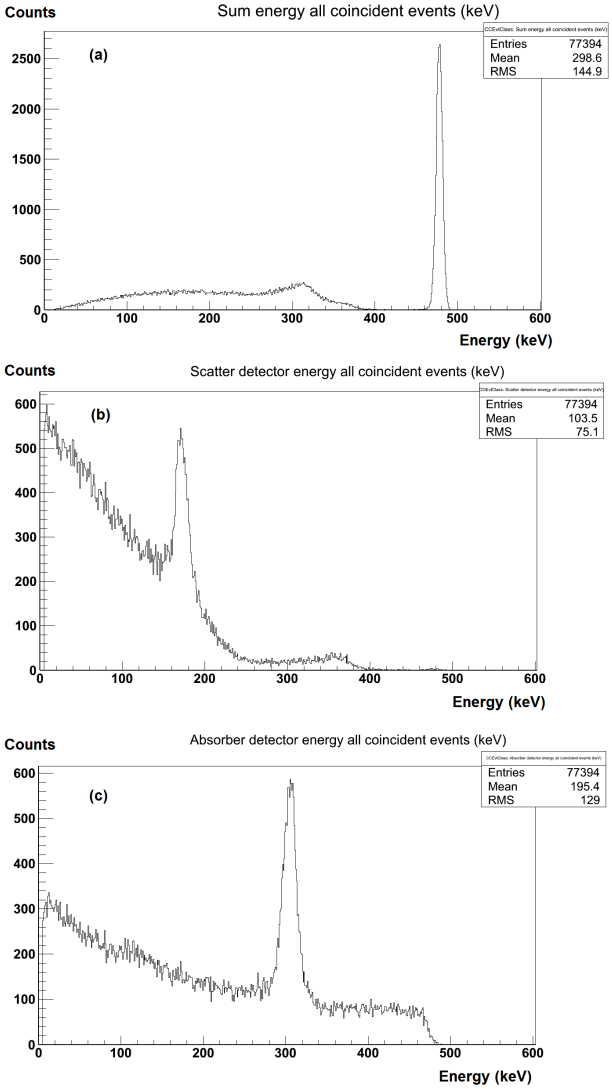

Figure 5.10: ROOT histogram of all coincident events - (0,0) position with 70,000,000 γ-rays - ROOT histograms showing the sum energy of all coincident events, scatter detector energy of all coincident events and absorber detector energy of all coincident events

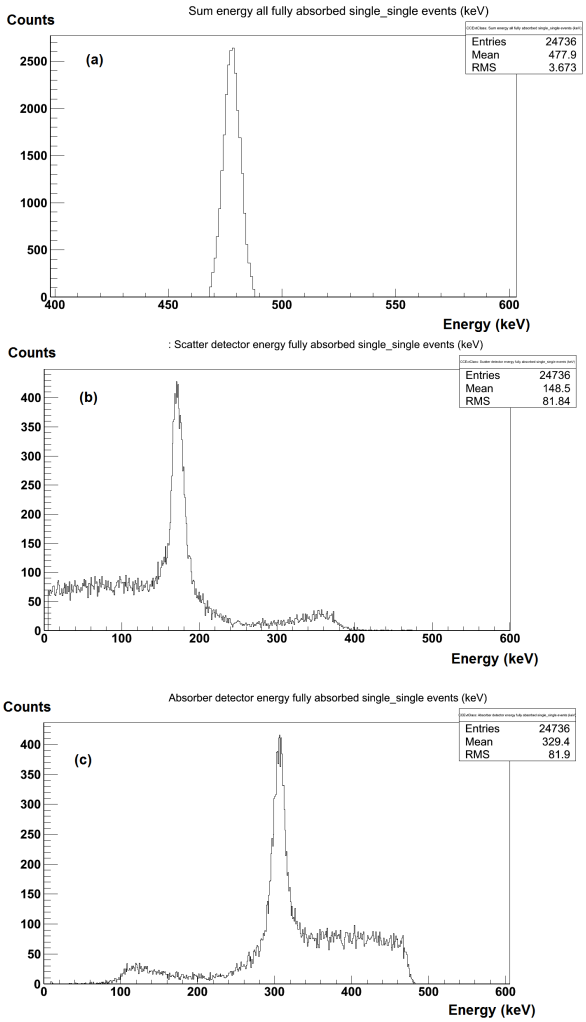

Figure 5.11: ROOT histogram of fully absorbed single/single events - (0,0) position with 70,000,000 γ-rays - ROOT histograms showing the sum energy of fully absorbed single/single events, scatter detector energy of fully absorbed single/single events and absorber detector energy of fully absorbed single/single events

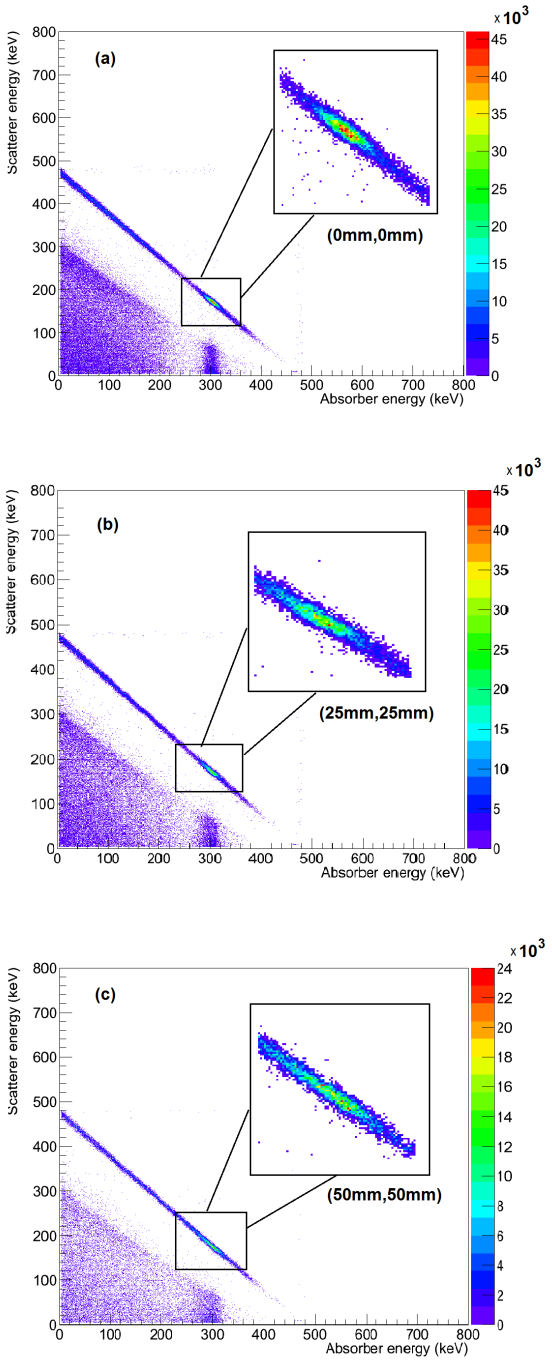

Figure 5.12: Matrix of deposited energy in scatter detector against deposited energy in absorber detector - Matrix representation of the energy deposited in the scatter detector against the energy deposited in the absorber detector; (a) for (0,0) position, (b) for (25,25) position and (c) for (50,50) position. The zoom shows the mean energy deposited in the scatter and absorber detector. The increasing scattering angle at (50,50) compared to the (0,0) position leads to greater energy deposition in the scatter detector.

5.5.4 Efficiency

The efficiency is a very important parameter as it shows how many cones are reconstructed for a given number of γ-rays. Hence the efficiency can be easily calculated as

$$\epsilon = \frac{N_{cones}}{N_{\gamma-rays}} \tag{5.1}$$

For the produced grid, 70,000,000 γ-rays are generated. Depending on the position of the point source, only a very small fraction of these γ-rays is actually used for the image reconstruction. This can be seen in table 5.1 . The efficiency is not fluctuating for a different number of γ-rays.

This seems like a tiny fraction that has been used for the reconstruction , but it can be explained as follows

1. The source is isotropic and hence the γ-rays are escaping in all directions. By taking the area of the sphere with a radius equal to the distance to the scatterer detector and dividing by the area of the detector, the fraction of γ-rays incident on the scatter detector can be found. By doing so, roughly 89% of the γ-rays do not hit the first detector. $\rightarrow$ 7,000,000 γ-rays left

2. More γ-rays are lost due to the attenuation in the scatter detector. This means some of the γ-rays lose their energy in the scatter detector and will not make it to the absorber detector. $\rightarrow$ 4,500,000 γ-rays left

3. More γ-rays are lost due to the scattering out of the detector. $\rightarrow$ 1,000,000 γ-rays left

x-position	y-position	No. of beams	Used no. of cones	% used
0	0	70000000	20990	0.030%
0	0	800000	232	0.029%
50	50	70000000	9896	0.014%
50	50	800000	110	0.014%

Table 5.1: Efficiency of Compton camera - The table shows the number of γ-rays and the number of cones used for the image reconstruction at two different positions. Only a very small fraction of cones used for the image reconstruction to emitted number of γ-rays

4. Another fraction of γ-rays is lost due to multiple interactions in one of the detectors. Only single/single interactions were taken into account, discarding all other types of events. $\rightarrow$ 350,000 γ-rays left

5. Another factor reducing the number of γ-rays and therefore number of cones for image reconstruction is the separation of the two detectors. Some γ-rays are scattered in the first detector, but do not reach the second detector. This is again a solid angle effect. $\rightarrow$ 100,000 γ-rays left

6. Finally, some of the incident γ-rays scatter out of the absorber detector. This reduces the number to 20,000 γ-rays

This derivation of γ-ray loss also indicates, what could in principle be improved to yield a higher ratio of cones to γ-rays. But one has to be aware that for example reducing the distance between the source and the first detector could lead to more uncertainties when reconstructing the image. It is therefore a trade off between number of cones and increase of error in position resolution. This will be shown in the next section.

5.5.5 Minimum Number of γ-rays for Image Reconstruction

A clinical treatment requires a short time period for the treatment to minimise unnecessary damage to the patient. Therefore the number of cones that are required for a good image reconstruction had to be found. It has been shown that a minimum number of 100 cones is sufficient for a good image reconstruction of a source. Various simulations were run, to find the minimum number of γ-rays to achieve this. It was found, that 800,000 γ-rays are required for this number of cones. Figure 5.13 shows the reconstruction of a point source at (0,0) with 800,000 γ-rays and it can be seen that the quality is significantly better than a reconstruction with 500,000 γ-rays as seen in figure 5.16.

Updated image reconstruction code An updated version of the Compton imaging reconstruction code has been used to investigate how the image quality could be improved. In Compton 3.6 the imaging space resolution (pixel size) can be defined

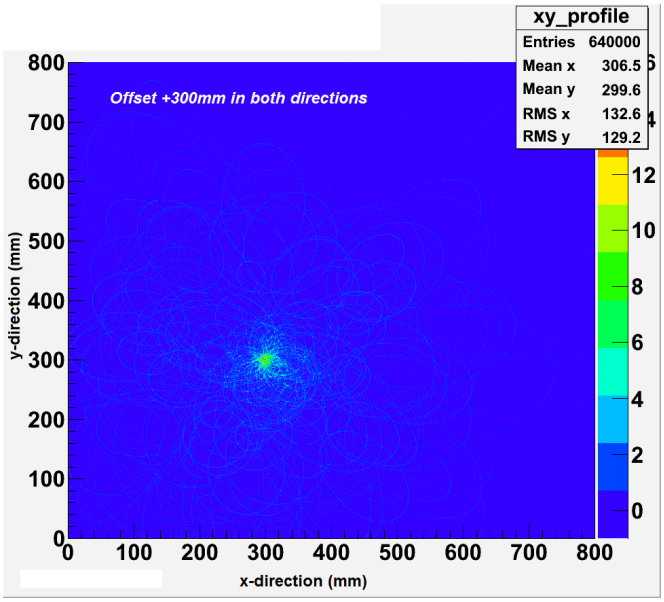

Figure 5.13: Image reconstruction - (0,0) position with 800,000 γ-rays - Image reconstruction of the source at the (0,0) position with 800,000 γ-rays.

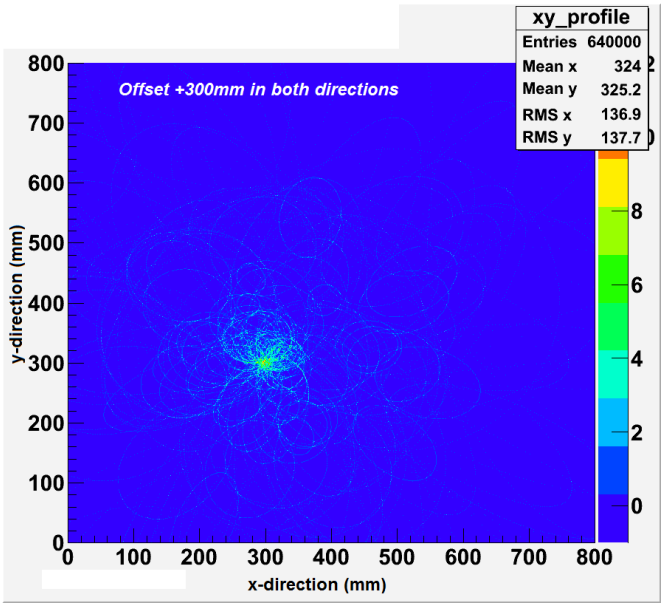

Figure 5.14: Image reconstruction - (25,25) position with 800,000 γ-rays - Image reconstruction of the source at the (25,25) position with 800,000 γ-rays.

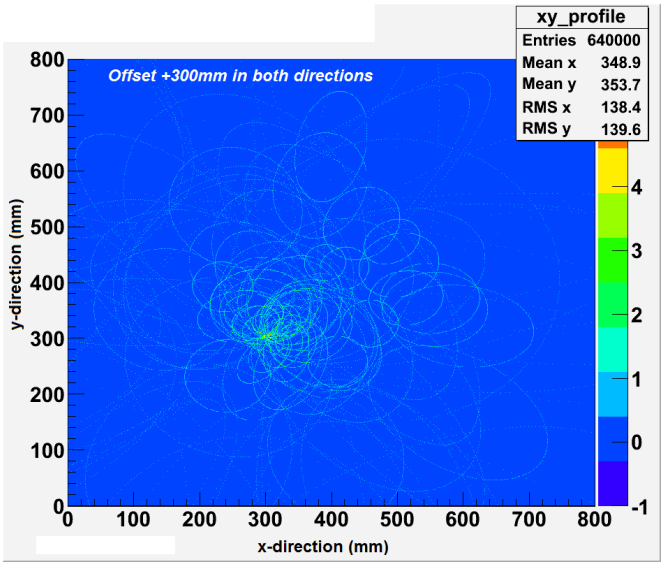

Figure 5.15: Image reconstruction - (50,50) position with 800,000 γ-rays - Image reconstruction of the source at the (50,50) position with 800,000 γ-rays.

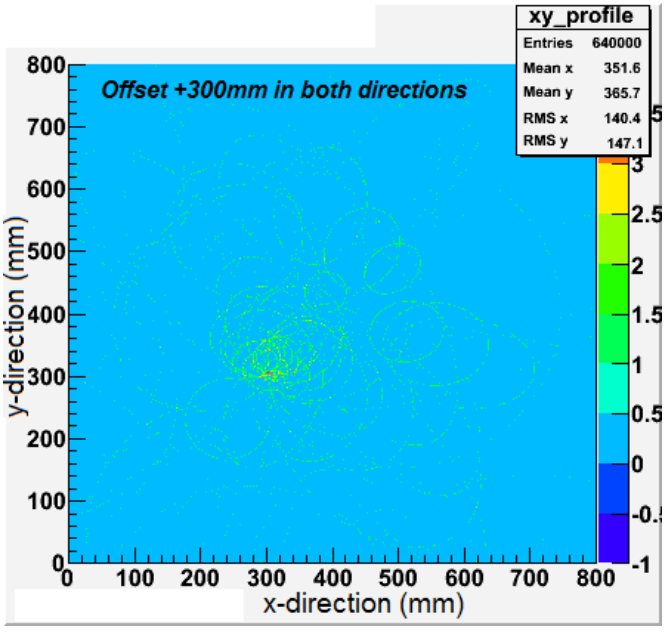

Figure 5.16: Image reconstruction - (50,50) position with 500,000 γ-rays - Image reconstruction of the source at the (50,50) position with 500,000 γ-rays.

[1]. A larger imaging space resolution gives a better image using fewer statistics. The updated code also allows to vary the number of points used to create a conic. Instead of one point drawn per degree (360 in total), multiple points can be drawn per degree. Figure 5.17 and 5.18 show the reconstruction of the images with 8 mm imaging space and five points per degree for 800,000 and 70,000,000 γ -rays respectively. The image quality for 70,000,000 does not increase, but the fit for 800,000 looks better.

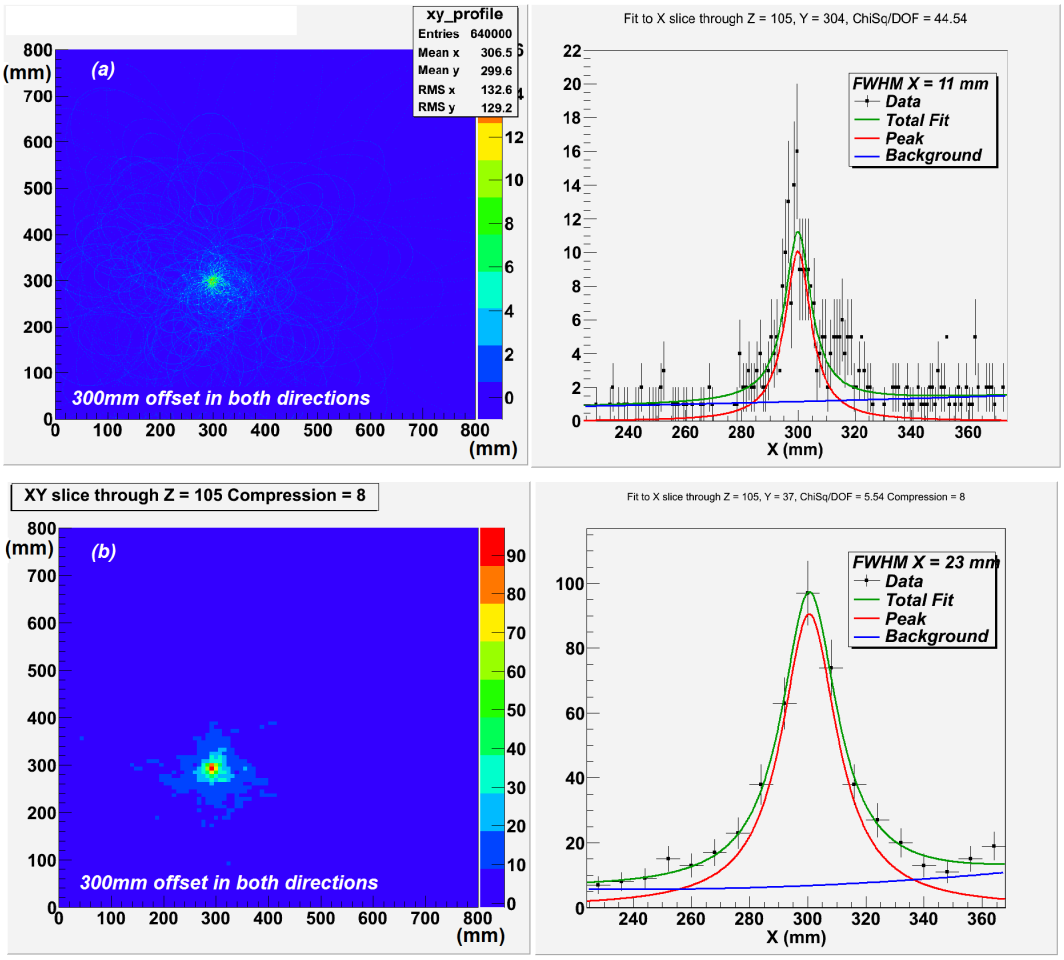

Figure 5.17: Updated image reconstruction - (0,0) position with 800,000 γ-rays - Updated image reconstruction of the (0,0) position with 800,000 γ-rays. The voxel size has been increased and more points on the perimeter of the cone base are produced.

[1]Compton 3.5 used a 1mm x 1mm pixel size

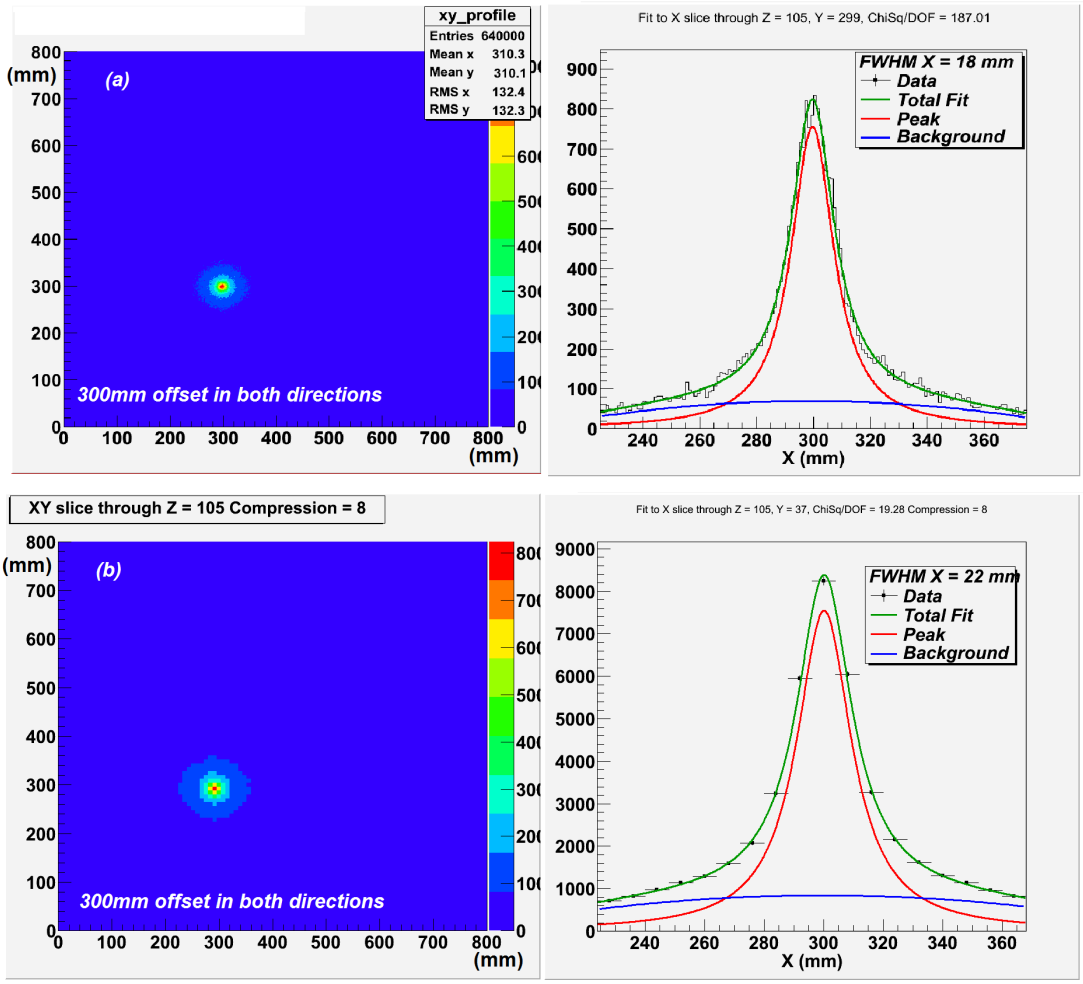

Figure 5.18: Updated image reconstruction - (0,0) position with 70,000,000 γ-rays - Updated image reconstruction of the (0,0) position with 70,000,000 γ-rays. The voxel size has been increased and more points on the perimeter of the cone base are produced.

5.6 Optimisation of Compton camera system

As previously shown, the efficiency [1] is very low. The Compton camera system has to be optimised, to increase the number of usable γ-rays. Several GAMOS simulations were utilised to determine the configuration of detectors which produce the maximum number of events. The optimisation of the detector configuration involved determining the ideal thickness of both scatter and absorber detector as well as the effect of taking into account multiple interaction events. The different variables were investigated with the other variables being kept constant.

5.6.1 Scatter Detector

In order to optimise the Compton camera imaging system for the boron energy at 478 keV, the thickness of the scatter detector was changed to investigate the number of cones reconstructed. For a better image reconstruction, this number has to be maximised. During the simulations, the detector separation was constant, so no solid angle effect would have an impact on the results. The analyser detector is a 60 x 60 x 20 mm thick germanium detector with 5 mm x 5 mm pixel sizes and only single/single events have been taken into account. The results can be seen in table 5.2. The simulations were carried out using the constant detector surface area of 60 mm x 60 mm and the two detectors were separated by 30 mm. As previously mentioned, HPGe [2] is a good detector material as it has a high cross section for the Compton scattering process. HPGe also offers an excellent energy resolution of around 2 keV at 478 keV [3] and the position resolution can be improved from the raw detector segmentation to 1 mm through the application of pulse shape analysis techniques.

As it can bee seen in figure 5.19 a scatter detector thickness of 10 mm gives the greatest number of counts for the boron energy. Beyond a thickness of 10 mm, the number of events decreases with increasing thickness. This is due to the increased probability of full absorption in a thicker detector, as photoelectric absorption is a very likely interaction mechanism.

[1] Yield of cones used for reconstruction for a given number of γ-rays
[2] HPGe = Hyper Pure Germanium Detector
[3] For simplicity an infinitely energy resolution of the detectors is assumed.

Thickness (mm)	No. total cones	No. used cones	% used
5	24750	21028	84,96%
7,5	29621	25321	85,48%
10	30943	26779	86,54%
12,5	30613	26731	87,32%
15	29343	25899	88,26%
17,5	27650	24640	89,11%
20	25565	22909	89,61%

Table 5.2: Optimum thickness of germanium scatter detector - The table shows the number of cones used for image reconstruction as the germanium scatter detector thickness is increased.

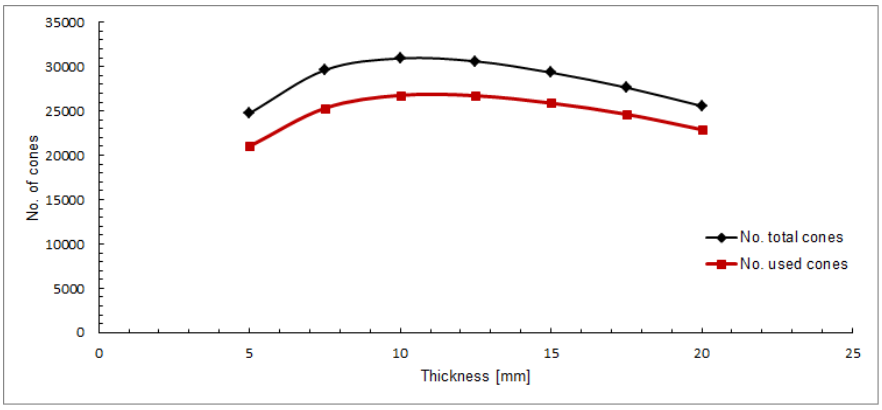

Figure 5.19: Optimum thickness of germanium scatter detector - The plot of the number of cones used for image reconstruction against scatter detector thickness peaks at around 10mm for germanium.

Thickness (mm)	No. total cones	No. used cones	% used
5	9286	8571	92,30%
7,5	11935	10949	91,74%
8	12404	11331	91,35%
10	14017	12809	91,38%
12,5	15480	14093	91,04%
15	16394	14925	91,04%
17,5	16866	15375	91,16%
20	16770	15271	91,06%

Table 5.3: Optimum thickness of silicon scatter detector - The table shows the number of cones used for image reconstruction as the silicon scatter detector thickness is increased.

Varying scatterer detector size to find ideal thickness of a silicon scatter detector With the same germanium detector and a silicon (Si) detector as scatter detector, the same simulations were run for a Si/Ge detector setup.

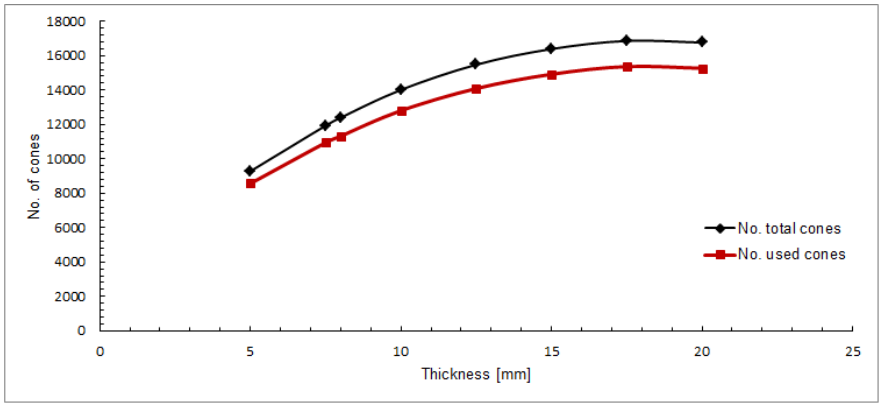

Figure 5.20: Optimum thickness of silicon scatter detector - The plot of the number of cones used for image reconstruction against scatter detector thickness peaks at around 17.5mm for silicon.

Figure 5.20 suggests that a thickness of 17.5mm gives the best results for the 478 keV photopeak.

Thickness (mm)	No. total cones	No. used cones	% used
10	30750	26625	86,59%
15	29175	25703	88,10%
20	25551	22871	89,51%
25	21378	19307	90,31%
30	17266	15701	90,94%
35	13825	12758	92,28%
40	10909	10055	92,17%
45	8546	7972	93,28%
50	6736	6303	93,57%
60	4007	3765	93,96%
70	2435	2299	94,41%
80	1394	1325	95,05%
90	815	775	95,09%
100	484	458	94,63%
150	41	38	92,68%
200	2	2	100,00%

Table 5.4: Optimum thickness of germanium absorber detector - The table shows the decrease in number of cones used for image reconstruction as the germanium scatter detector thickness is increased.

5.6.2 Absorber Detector

Simulations were performed to find the total thickness of the absorber detector, which leads to a full absorption of the incident 478 keV γ-ray. As GAMOS is set by default to only record single/single interactions, the number of recorded cones should decrease as the scatterer thickness increases. The thicker the detector, the more likely full absorption of the incident γ-rays is and hence less γ-rays will escape the scatter detector.

As seen in table 5.4, the number of cones approaches zero towards a scatter detector thickness of about 200 mm. At the moment, 90 mm thick germanium detector can be achieved. For economic reasons, a 40 mm thick detector is considered to be sufficient for BNCT giving the best trade-off between number of events and cost of the detector.

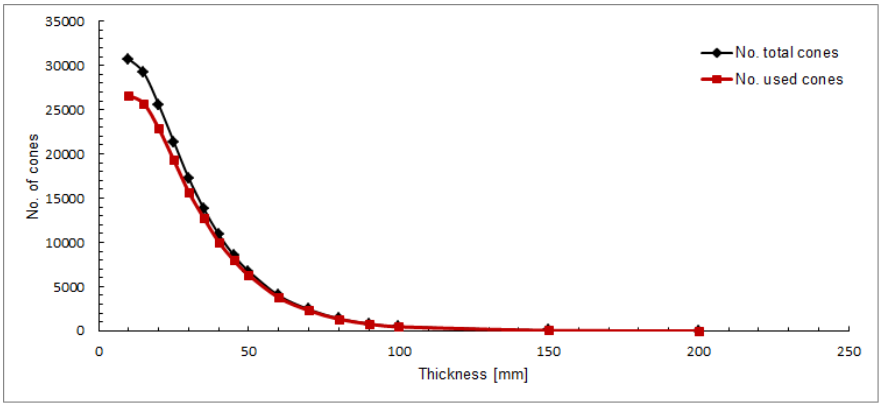

Figure 5.21: Optimum thickness of germanium absorber detector - This plot shows the decrease in number of cones used for image reconstruction as the germanium scatter detector thickness is increased. The incident γ-rays are fully absorbed before escaping the scatter detector. The curve approaches at around 90 mm, which is therefore the optimum thickness for a germanium absorber detector.

5.6.3 Multiple Interactions

The effect of multiple interactions in the detectors has been studied. So far, only so called single/single interactions were taken into account as they are easy to process and simple to use for the cone reconstruction. As previously explained, single/single means, that the γ-ray has to scatter once in the first detector before being fully absorbed in the second detector without further scattering. This is of course not the only way, an incident γ-ray can undergo an interaction. A single/double events describes an γ-ray, that is being Compton scattered in the first detector, undergoing another scattering in the second detector before being fully absorbed. An illustration of this can be seen in figure 5.2. Multiple interaction events could be used and most likely increase the quality of the reconstructed images. Figure 5.22 shows, how the two interactions in the second detector can be averaged out to a single interaction point and then being processes as a normal single/single event. The simulations were performed for three different positions, at (0mm,0mm), (25mm,25mm) and (50mm,50mm). In the first set of simulations the detector setup is identical with the setup used in the section "Position Resolution". Hence, the scatter and absorber detector have dimensions of 60 mm x 60 mm x 5mm and 60 mm x 60 mm x 20 mm, respectively.

The tables 5.5, 5.6 and 5.7 show that only around 35% of the events are single/single.

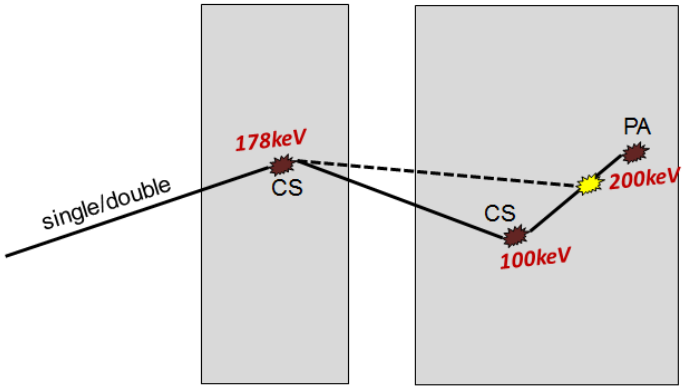

Figure 5.22: Reconstruction of single/double event into a single/single interaction - This shows how two interactions are combined in the absorber detector to be represented as a single interaction point. The interactions are averaged out according to their energy. In this case the ratio is 2:1 between photoelectric absorption (PA) and Compton scattering (CS)

Event Classification	No. of events	% of total
Single/Single	26134	35,38%
Single/Double	20970	28,39%
Single/Multiple	13146	17,80%
Double/Single	7921	10,72%
Double/Double	2853	3,86%
Double/Multiple	857	1,16%
Multiple/Single	1575	2,13%
Multiple/Double	367	0,50%
Multiple/Multiple	51	0,07%

Table 5.5: Event distribution - (0,0) position with 70,000,000 γ-rays - The table shows the distribution of the various events for the (0,0) position with 70,000,000 γ-rays.

Event Classification	No. of events	% of total
Single/Single	20479	35,50%
Single/Double	16224	28,12%
Single/Multiple	10129	17,56%
Double/Single	6179	10,71%
Double/Double	2332	4,04%
Double/Multiple	730	1,27%
Multiple/Single	1270	2,20%
Multiple/Double	286	0,50%
Multiple/Multiple	65	0,11%

Table 5.6: Event distribution - (25,25) position with 70,000,000 γ-rays - The table shows the distribution of the various events for the (25,25) position with 70,000,000 γ-rays.

Event Classification	No. of events	% of total
Single/Single	12019	36,63%
Single/Double	9068	27,64%
Single/Multiple	5161	15,73%
Double/Single	3594	10,95%
Double/Double	1470	4,48%
Double/Multiple	465	1,42%
Multiple/Single	772	2,35%
Multiple/Double	214	0,65%
Multiple/Multiple	45	0,14%

Table 5.7: Event distribution - (50,50) position with 70,000,000 γ-rays - The table shows the distribution of the various events for the (50,50) position with 70,000,000 γ-rays.

Therefore around 65% of the events get lost.

The simulations were run again to investigate the event distribution with the ideal detector setup consisting of a 10 mm thick scatter detector and 90 mm thick scatter detector. As shown in the tables 5.8, 5.9 and 5.10, the fraction of different multiple interactions events varies quite drastically from the 5 mm/20 mm setup. Only around 25% of the events are single/single. This can be explained, as a bigger analyser detector increases the probability of detecting gamma rays that undergo multiple scattering before being photo-electrically absorbed. As it can be seen in figure 5.23 the percentage of events with only one interaction in the scatter detector and one or more interactions in the absorber detectors is very similiar. This is good, as the detector has to be thin enough, as otherwise γ-rays may be absorbed in the first detector and would not give rise to a detection.

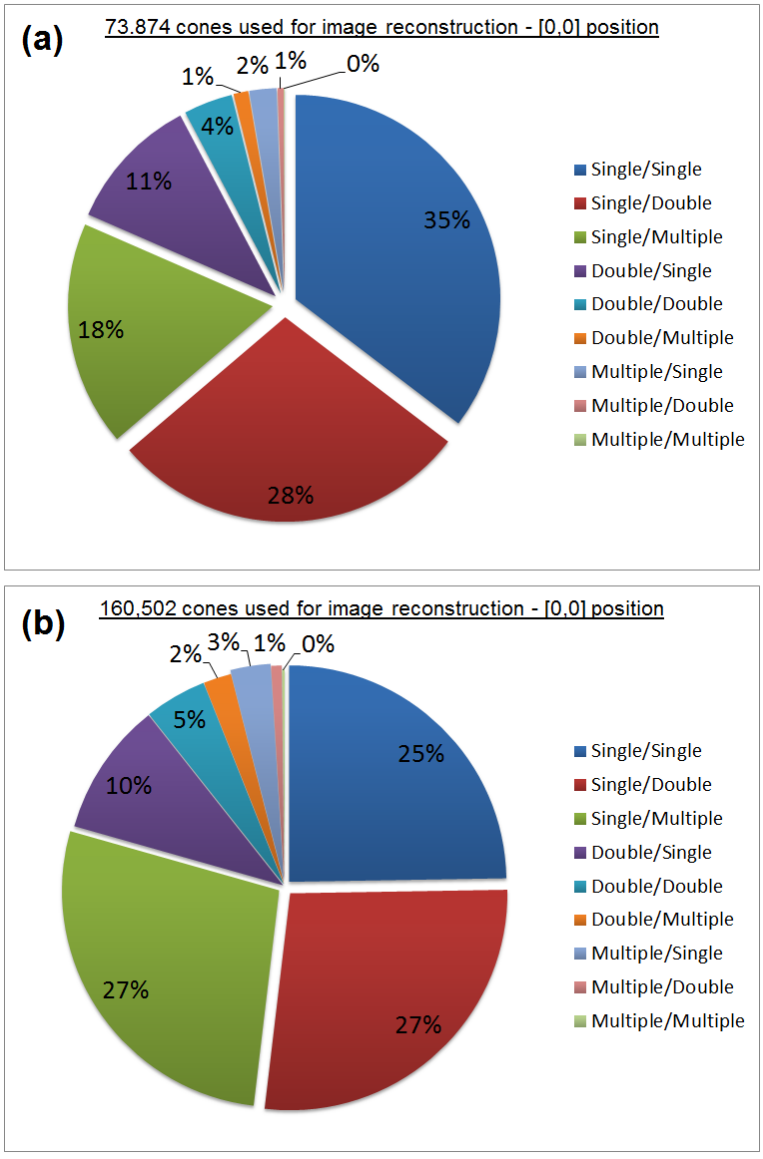

Figure 5.23: Comparison of event distribution for 5 mm/20 mm setup and 10mm /90 mm setup for the (0,0) position - The pie charts show the event distributions for the 5 mm/20 mm setup and 10mm /90 mm setup for the (0,0) position

Event Classification	No. of events	% of total
Single/Single	39706	24,74%
Single/Double	43565	27,14%
Single/Multiple	44165	27,52%
Double/Single	15976	9,95%
Double/Double	7414	4,62%
Double/Multiple	3333	2,08%
Multiple/Single	4789	2,98%
Multiple/Double	1259	0,78%
Multiple/Multiple	295	0,18%

Table 5.8: Event distribution - (0,0) position with 70,000,000 γ-rays with ideal detector setup - The table shows the distribution of the various events for the (0,0) position with 70,000,000 γ-rays with the ideal detector setup; 10 mm germanium scatter detector and 90 mm absorber detector.

Event Classification	No. of events	% of total
Single/Single	31041	25,14%
Single/Double	32969	26,70%
Single/Multiple	33107	26,82%
Double/Single	12565	10,18%
Double/Double	5904	4,78%
Double/Multiple	2803	2,27%
Multiple/Single	3816	3,09%
Multiple/Double	1002	0,81%
Multiple/Multiple	251	0,20%

Table 5.9: Event distribution - (25,25) position with 70,000,000 γ-rays with ideal detector setup - The table shows the distribution of the various events for the (25,25) position with 70,000,000 γ-rays with the ideal detector setup; 10 mm germanium scatter detector and 90 mm absorber detector.

Event Classification	No. of events	% of total
Single/Single	18264	27,10%
Single/Double	17318	25,70%
Single/Multiple	15642	23,21%
Double/Single	7536	11,18%
Double/Double	3667	5,44%
Double/Multiple	1767	2,62%
Multiple/Single	2335	3,47%
Multiple/Double	677	1,00%
Multiple/Multiple	182	0,27%

Table 5.10: Event distribution - (50,50) position with 70,000,000 γ-rays with ideal detector setup - The table shows the distribution of the various events for the (50,50) position with 70,000,000 γ-rays with the ideal detector setup; 10 mm germanium scatter detector and 90 mm absorber detector.

5.6.4 Detector Separation

The distance between the scatter and absorber detector was varied to find the ideal separation. It is useful to investigate the influence on sensitivity of varying the separation distance to consider the advantages and disadvantages of a higher yield in events over larger uncertainties in the position resolution. The closer the two detectors are placed to each other, the greater the yield in cones is. But the increase in number of cones comes with an increase of uncertainty in the position resolution. Therefore it is a trade off between position resolution and efficiency.

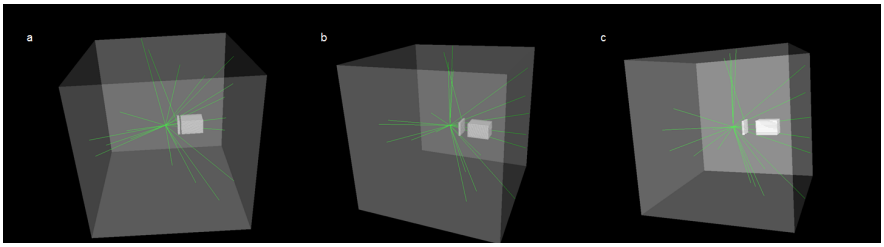

Figure 5.24: Optimised Compton camera setup with varying detector separation - This shows the optimised detector setup with varying detector separation. The FWHM is plotted alongside the number of cones.

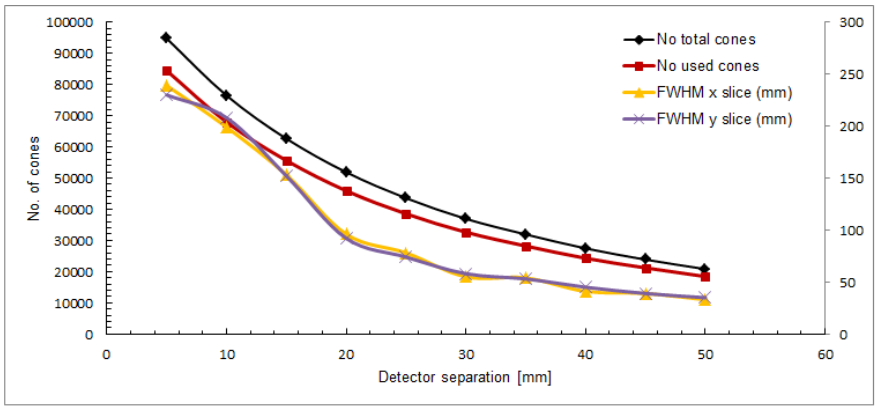

Figure 5.25: - This shows the detector setup and its various separations

Figure 5.25 suggests that the ideal separation is around 30 mm which gives a sufficient number of cones while the uncertainties are relatively small.

5.7 Summary of Results

The optimisation of a Compton camera system for its use during Boron Neutron Capture Therapy with γ-rays with 478 keV energy has been carried out using various GAMOS simulations. The efficiency of the Compton camera system has been optimised by investigating scatter and absorber detectors with different thicknesses and studying the improvements by taking into account multiple interactions. The results have shown that the highest yield of cones per γ-rays is achieved with a configuration of a 10 mm thick HPGe scatter detector placed 30 mm, which is practically possible, away to a 90 mm thick HPGe analyser detector. For economic reasons, a 40mm thick analyser detector is assumed to be sufficient. Utilising events from multiple interactions by employing advanced event processing and image reconstruction techniques will possibly improve the overall imaging of the optimised Compton camera configuration significantly. On average 175 keV is deposited in the scatter detector and the other 305 kev is deposited in the analyser detector. This shifts to more deposited energy in the scatter detector when the source is moved away from the center of the detector, as a higher scattering angle leads to more energy deposition.

For further optimisation it is recommended to study other materials at this energy as detector material . Si(li) for example provide excellent energy and position resolution and the contribution of Doppler broadening is a lot lower than that of HPGe due to its lower atomic number. Hence, Si(Li) could be a potentially a good choice of material for scatter detector. For the absorber detector a material like caesium iodine or cadmium zinc telluride might be better suited for this purpose. This has to be further investigated.

All the analysis has been carried out with two detectors with the same planar dimensions of 60 x 60 mm for both the scatter and the absorber detector. It would be recommended to investigate how the number of incident events can be improved as the planar dimensions of the absorber are increased relative to the those of the scatter detector. Obviously, the solid angle coverage would increase as the absorber area is increased. The solid angle has been identified as the factor that influences the efficiency at most. The information acquired from such an investigation would be beneficial in examining the trade off between the cost of a larger absorber detector with the increase in sensitivity due to the larger solid angle coverage.

6

Boron Spectroscopy and Neutron Detection

6.1 Objective

The previous chapter evaluated the image reconstruction of a point source with a given number of incident γ-rays. For the Compton camera system to be feasible during Boron Neutron Capture Therapy, a sufficient amount of γ-rays have to be collected in a small volume as this is required during clinical treatment. Therefore, an experiment was set up to investigate the number of counts in the characteristic 478 keV boron peak and to estimate the number of thermal neutrons, when a boron containing material is exposed to a neutron source.

6.2 Experimental Setup

The experiment was carried out in the neutron laboratory in the Chadwick building and the setup is shown in figure 6.1. A neutron source, which can be freely moved from a thermal position to a high energy position is placed in a water tank. In both positions thermalised neutrons [1] are targeted on a ^{10}B-containing CH_2-sheet, where they are captured and emit characteristic 478 keV γ-rays. In the thermal energy position, the solid angle coverage of the detector is a lot smaller than in the high energy position. A germanium detector is used for the γ-ray spectroscopy and a ^3He-detector records the

[1] In the high energy position neutrons are thermalised due to collisions in the water and due to backscattering in the tank

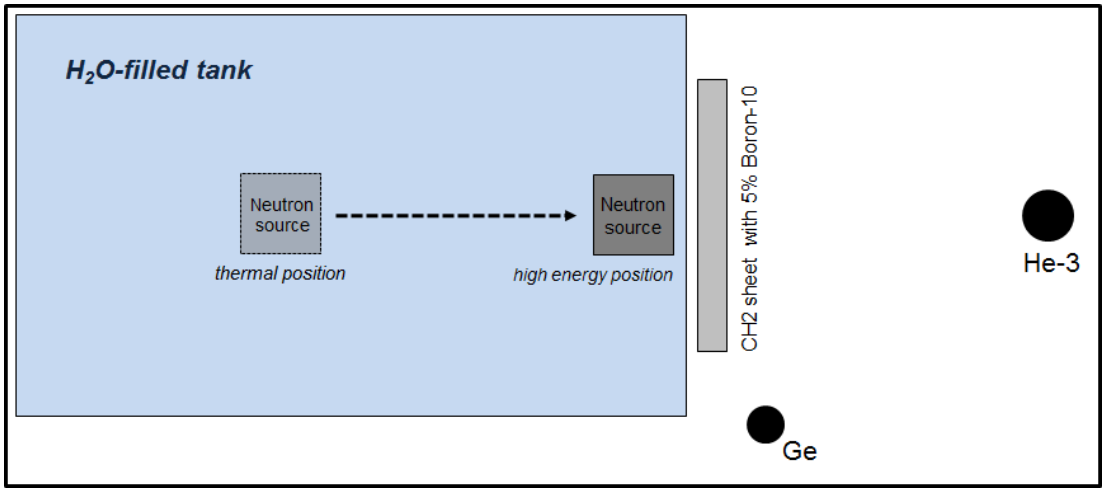

Figure 6.1: Experimental setup in neutron laboratory - This is a schematic illustration of the experimental setup in the neutron laboratory.

Sheet	Area
1	5 cm x 5 cm
2	25 cm x 29.5 cm
3	51 cm x 59 cm
4	51 cm x 90 cm
5	60 cm x 101 cm

Table 6.1: Sizes of the CH_2 sheets with 5% ^{10}B - Five different sized CH_2 sheets with 5% ^{10}B were placed in front of the neutron source.

thermal neutron flux. The 2.5 cm thick CH_2-sheets have a 5% concentration of ^{10}B and were cut in five different sizes to investigate the number of counts in the boron peak at 478 keV. Table 6.1 shows the sizes of the CH_2 sheets.

The sheets were placed in front of the water tank and centered relative to the neutron source. The ^3He-detector is situated around a meter away from the CH_2-sheets and the germanium detector is positioned next to the water tank. The germanium detector is connected in series with a Preamplifier, Amplifier, Analog-to-Digital Converter and Multi Channel Analyser. The Multi Channel Analyser is read with the program package MAESTRO. The ^3He-detector is set-up in a similar manner.

6.3 Equipment

6.3.1 Neutron Source

The neutron lab is equipped with an Americium-Beryllium (Am/Be) neutron source, which is used in this experiment. It is a small-size source and produces fast neutrons via a reaction in which the beryllium absorbs an alpha and emits a neutron; the neutrons are products of the reaction between the beryllium and the 5.5 MeV alpha particles emitted by the decaying americium nuclei. The neutron source in the water tank has a activity of 0.5 Curie, which equals to $1 * 10^6 \frac{neutrons}{second}$. The process of the neutron activation is

$$^{241}Am \rightarrow ^{237} Np + \alpha \tag{6.1}$$

$$\alpha + ^{9} Be \rightarrow ^{12} C + n\text{- fast neutron emitted} \tag{6.2}$$

The Q-value of this reaction is 5.7 MeV.

Neutron Moderation The neutrons are moderated as explained in chapter 2. Water is a cheap and convenient moderator [1] as it has a low atomic number and therefore does not absorb the incident neutron. A series of collisions with the protons in the moderator ensure that neutrons reduce their energy. After many collisions the energy of the neutron is comparable to the thermal energy of the water tank $\sim$ kT $\sim$ 0.025 eV.

Neutron Shielding To protect personnel from the biological effects of neutrons a neutron shielding is necessary. Thermal neutrons are best absorbed with great effectiveness by thin layers of boron or cadmium with large cross sections. Fast neutrons are more difficult to shield against, as the cross sections are much lower at high energies. Inelastic scattering or absorption may again produce potentially hazardous γ-rays; for example, neutron capture in hydrogen releases a 2223 keV γ-ray. Thus, an effective radiation shield consists of a combination of materials. Hydrogenous or other low-A materials, to moderate the neutrons, thermal neutron absorbers; and a high-Z materials to absorb γ-rays. Therefore a polyethylene sheet with added boron was placed behind the neutron source and a cadmium sheet shielded the neutron source to prevent radiation damage in the surroundings.

[1] Heavy water would be ideal, but only available at high cost

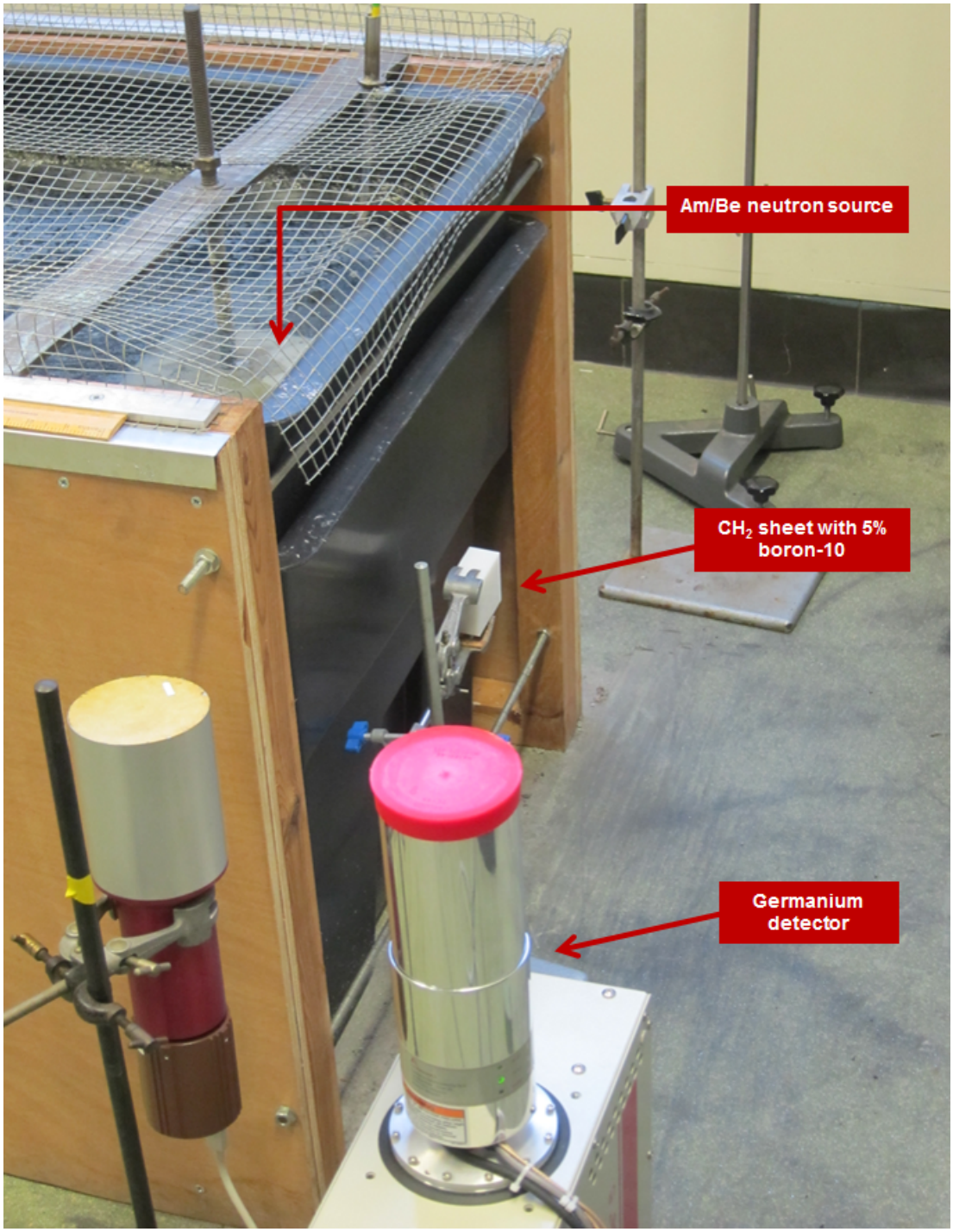

Figure 6.2: Experimental set-up in the neutron laboratory - The picture shows the experimental set-up in the neutron laboratory. The Am/Be is in the high energy position close to the edge of the tank. The CH_2-sheet is centered in front of the neutron source. The sheet seen on this picture is 5x5cm. The germanium detector (red cap) is placed next to the tank.

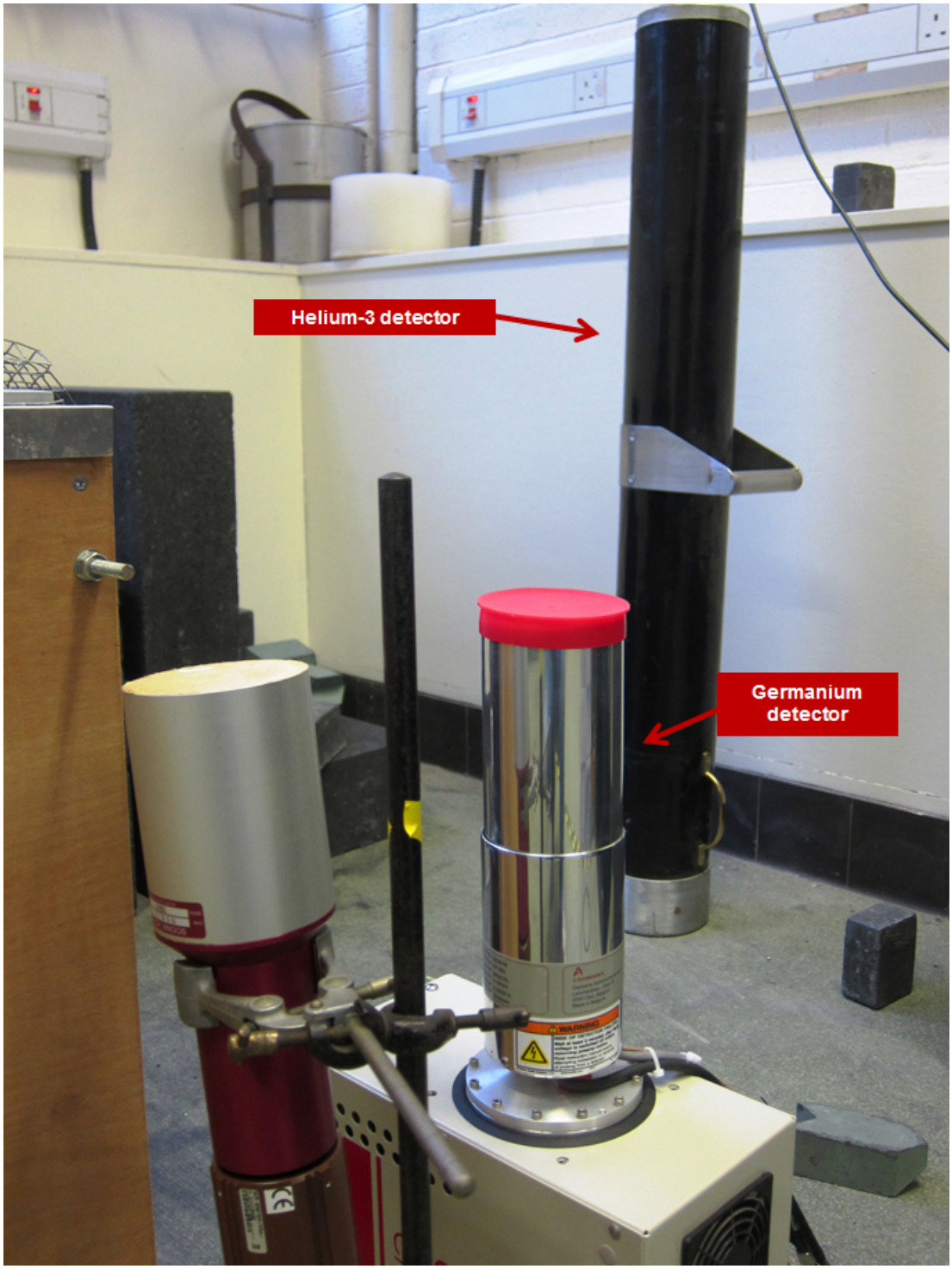

Figure 6.3: Helium-3 detector and germanium detector - The picture shows the experimental set-up in the neutron laboratory. The helium-3 detector is placed about a meter behind the watertank. The germanium detector (red cap) is placed next to the tank.

Model Number	BE2020
Area (cm2)	20
Thickness (mm)	20
Typical Rel. Eff. (%)	9
FWHM (keV) at 5.9keV	0.35
FWHM (keV) at 122keV	0.65
FWHM (keV) at 1332keV	2.00
Endcap diameter (mm)	76

Table 6.2: Characteristics of BEGe - The table shows the characteristics of the germanium detector.

Source	Characteristic peak [keV]
Americium	60
Cobalt	1173.2 & 1332.5
Cesium	662

Table 6.3: Radioactive sources for calibration - Characteristic γ-rays of the sources used for the calibration of the germanium detector.

6.3.2 Germanium Detector

Detector characteristics A Broad Energy Germanium Detector (BEGe) was used during this experiment, which is optimised to cover the energy range of 3 keV to 3 MeV. The BEGe has a short, fat shape which greatly enhances the efficiency below 1 MeV and offers a excellent energy resolution. Table 6.2 shows the properties of the used detector.

Calibration The germanium detector has been calibrated before the experiment was conducted. Three radioactive source, Americium (^{241}Am), Cobalt (^{60}Co) and Cesium (^{137}Cs) were placed next to the germanium detector and a spectrum was collected with sufficient statistics. Table 6.3 shows the characteristic γ-ray peaks of the calibration sources, which can be easily identified. By identifying the peaks in MAESTRO the detector is calibrated.

Channel selection in MAESTRO The number of channels for the given energy range in MAESTRO has to be chosen carefully between 2k and 16k channels to get an

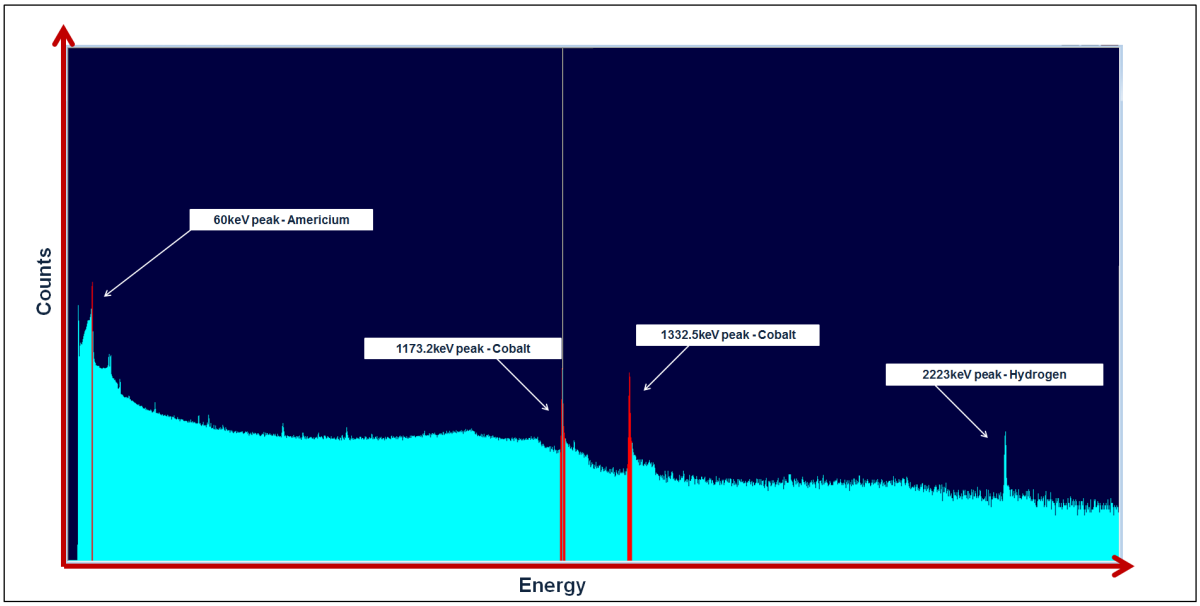

Figure 6.4: Calibration with Am and Co - The characteristics peak can easily be identified on this spectrum

adequate resolution for the calibration and the experiment. On the one hand, information on centroids and areas would be difficult to extract if the number of channels is too low. On the other hand, fewer counts per channel lead to greater uncertainty of the channel content. For this experiment, 8k channels were found to be the best setting.

Dead Time In nuclear detector systems, the dead time is the time after each event in which the system is not able to record another event if it happens. For example the readout and storage of the event, especially in detection systems with large number of channels contributes to the total dead time. From the total time a detection system is running, the dead time must be subtracted to obtain the live time of the experiment and thus obtain the correct value for the number of counts per time period.

6.3.3 Helium-3 Detector

The helium-3 detector that has been used in the experiment to detect the thermal neutrons has a pressure of 2 atm and is around one meter long. The tube has a diameter of 2 inch and is surrounded by a 2 mm thick stainless-steel wall. It operates at a voltage of around 1100V and is enriched with 5% argon.

6.4 Experiment

For each sheet a spectrum is collected for 18 hours (live time) for both the high energy and low energy position of the source. This is long enough for good statistics and gives a sufficiently large number of counts in the peaks of interest at 478 keV and 2223 keV. After all the spectra for the sheets have been recorded, background spectra are taken to analyse other contributions to the recorded spectra.

6.5 Results

6.5.1 Germanium Detector Spectra

A typical spectrum collected by the germanium detector can be seen in 6.6. The characteristic peak at 478 keV and the hydrogen peak at 2223 keV are easily identified.

Background radiation arises from cosmic radiation that continuously bombards the earth's atmosphere and natural radioactivity in the environment gives rise to various peaks. The most important contributions come from potassium, thorium and uranium and the long decay chains of thorium and uranium. Natural potassium contains 0.012% of ^{40}K, which decays with a $1.26x10^9$ year half-life emits a γ-ray with 1.460 MeV energy (11% branching fraction).
Figure 6.5 shows a γ-ray spectrum recorded over 170 h (2). Thorium, uranium, and radium are all members of long decay chains involving the daughter products that emit a mixed spectrum of alpha, beta and gamma-rays. The following daughter activities can be identified: in the thorium series ^{228}Ac, ^{224}Ra, ^{212}Bi, ^{212}Pb and ^{028}Tl. In the uranium series ^{226}Ra, ^{214}Pb and ^{214}Bi. The detection equipment and shielding is also a potential source of background radiation, especially ^{40}K is present in many materials and the 1.46 Mev γ-ray line can easily be identified. The 2.61 MeV, originating in the decay chain of ^{232}Th, is also an easily detectable peak. There is also a contribution of source-related background with the most significant processes of Compton backscattering of the primary γ-rays, and the generation of secondary annihilation photons and characteristic X-rays through pair production or photoelectric absorption. Most of the peaks arising from the background have been identified on the measured spectrum col-

lected with the germanium detector (Figure 6.6).

Another interesting feature that can be observed in the γ-ray spectrum is induced by the Am/Be neutron source. During the decay of the bound-excited state of $^{*12}C$, $(\alpha +^{9} Be \rightarrow^{*12} C + n)$, a 4.4 MeV photon is produced. The 3.9 and 3.4 MeV peaks are the single and double escape peaks of the this photon. The detector itself also gives rise to a characteristic peak when interacting with the neutrons. Figure 6.7 shows a γ-ray at 692 keV that is created due to the scattering to the first excited state of ^{72}Ge as it interacts with the incoming neutron. The ground state and the first excited have spin parity of 0^{+} and therefore the energy is the sum of the conversion electron and the recoiling nucleus. Thus, the minimum energy of the peak is 692 keV, but it drifts towards higher energies the more energetic the recoiling nucleus is.

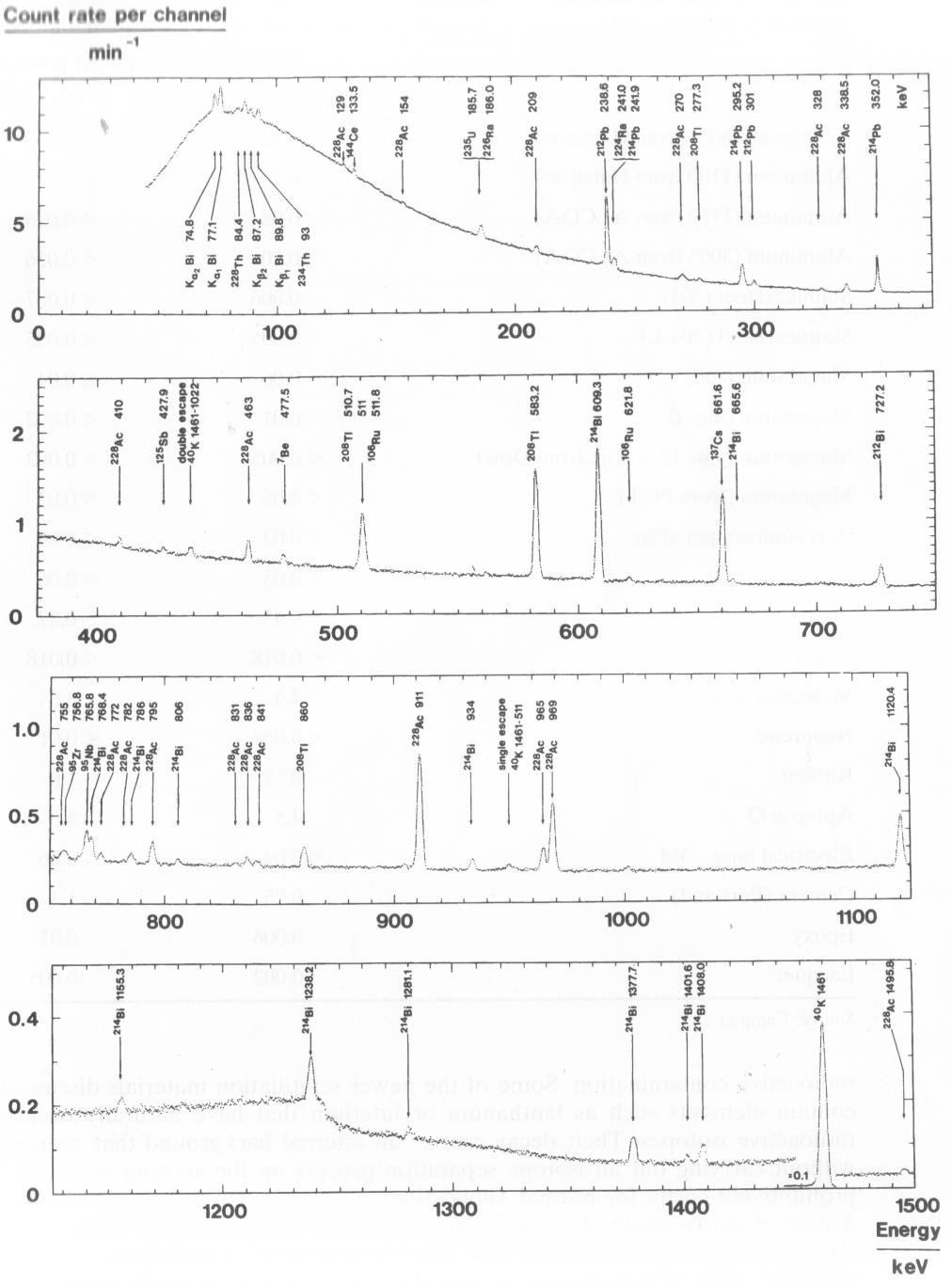

Figure 6.5: Background radiation in germanium detector - A terrestrial γ-ray spectrum recorded over 170 h using a 60 cm^3 germanium detector mounted 1 m above the ground.

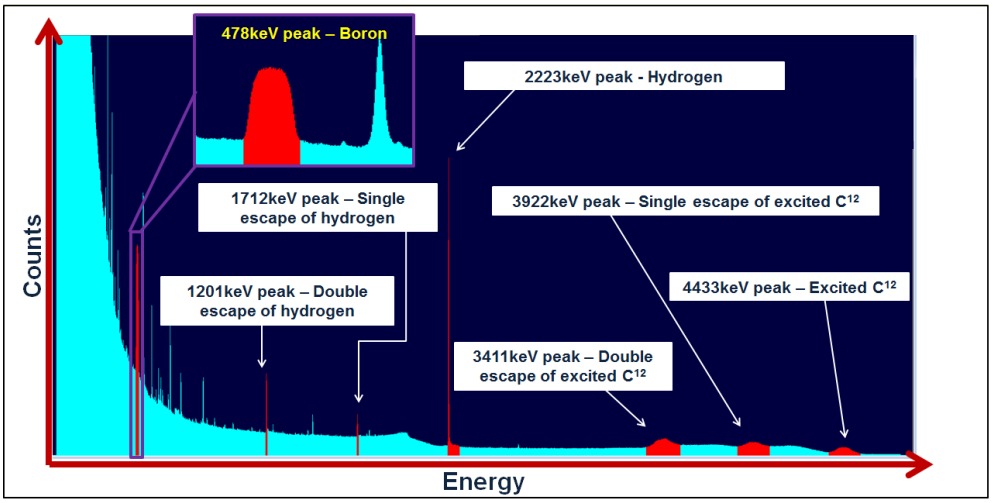

Figure 6.6: Typical germanium spectrum - This is a typical γ-ray spectrum collected by the germanium detector. The boron peak at 478keV and the hydrogen peak at 2223keV (and its single and double escape peaks) are clearly visible. At the higher end of the spectrum, the broad peak of excited C12 at 4433 keV and its single and double escape peaks can be identified. The boron peak is Doppler broadened, which is caused by the decay of neutron captured ^{10}B.

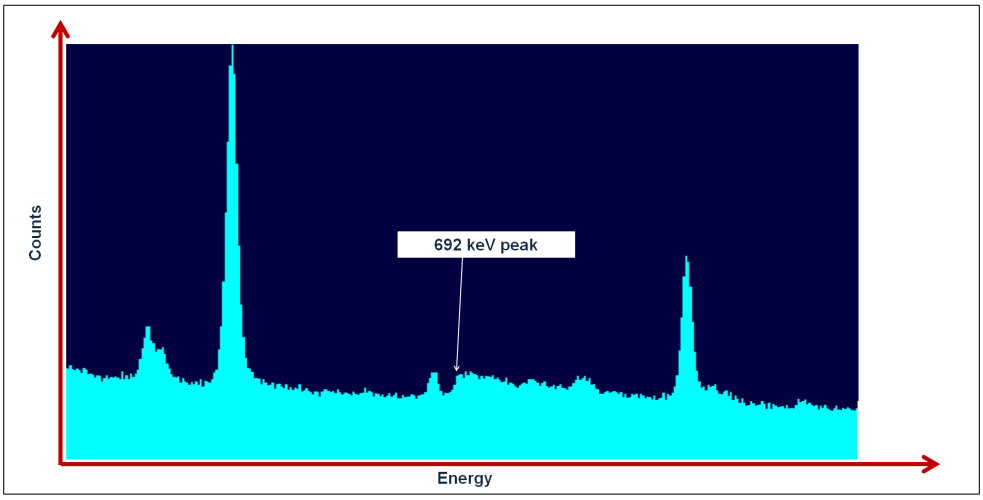

Figure 6.7: 692keV peak in the γ-ray spectrum - This peak at 692 keV correspond to the interaction of the neutrons with the germanium.

Full Width Half Maximum The Full Width Half Maximum (FWHM) of several peaks of the γ-ray spectrum was plotted against energy to investigate the effects on the energy resolution. The boron peak has a significantly higher FWHM as the table 6.4 shows. This can be explained with the Doppler broadening phenomenon (see next section). The peak arising from the excited ^{12}C and its single and double escape are also very large and have been discarded in figure 6.8.

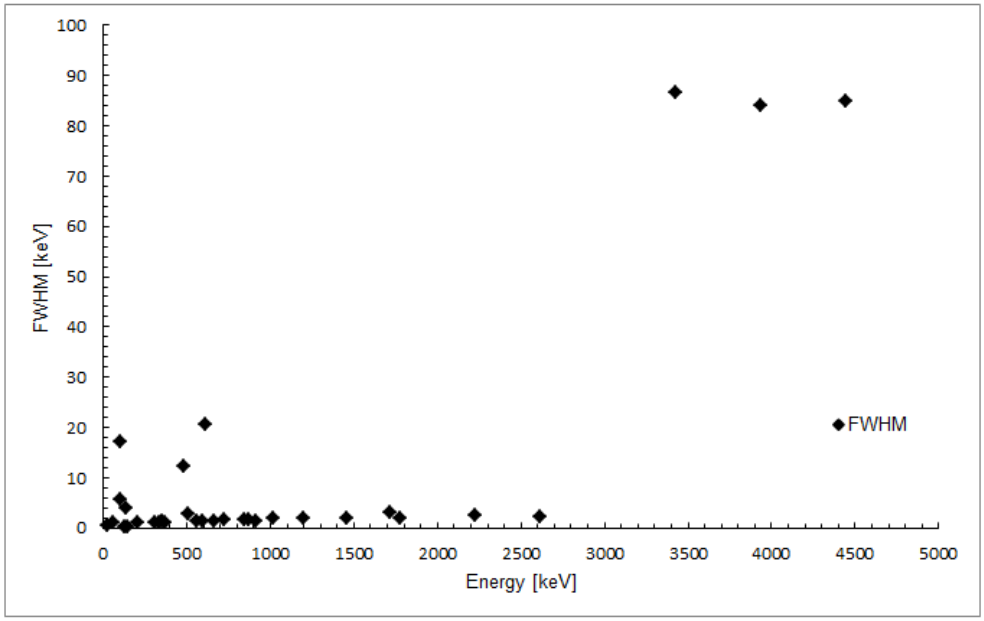

Figure 6.8: FWHM vs energy discarding higher energies - A plot of the FWHM against energy for several peaks discarding the broadened peaks at higher energies.

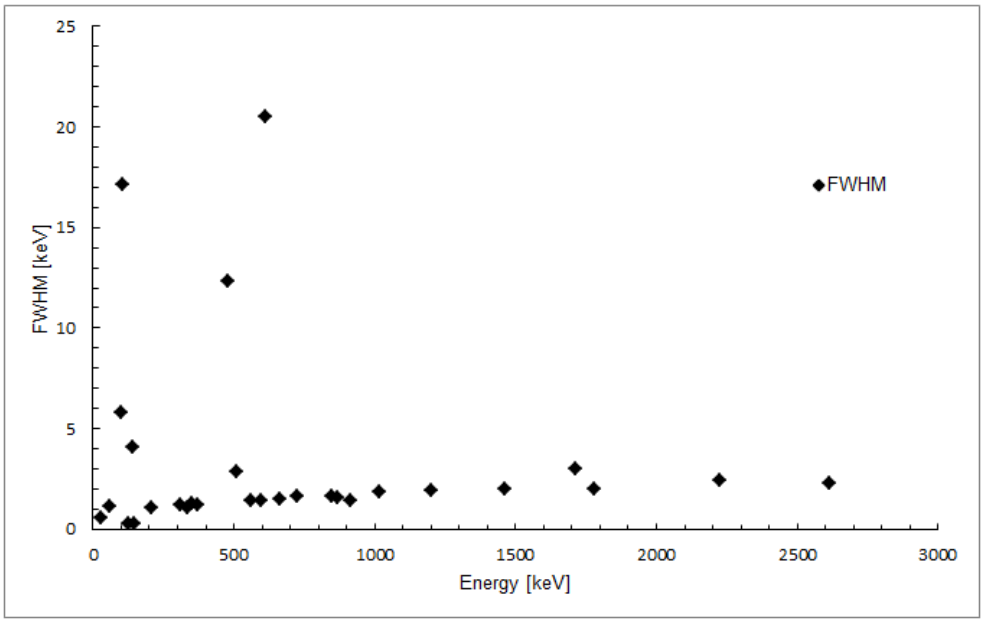

Figure 6.9: FWHM vs energy - A plot of the FWHM against energy for several peaks

Peak (keV)	FWHM	FWTM	FWTM/FWHM	Net area	ΔNet area
26.86	0.55	1.03	1.873	75036604	41937
60.09	1.12	4.83	4.313	12365481	8404
99.78	5.80	0.59	0.102	1226304	3663
103.80	17.14	0.82	0.048	1061966	2053
126.00	0.29	0.53	1.828	67568	603
140.44	4.07	0.82	0.201	39831	873
146.92	0.29	0.53	1.828	1160	426
208.90	1.06	1.82	1.717	148888	1048
312.85	1.19	2.22	1.866	134843	1123
336.38	1.07	1.63	1.523	77413	626
353.21	1.27	1.49	1.173	15381	721
369.60	1.21	4.00	3.306	54014	1222
478.78	12.33	13.59	1.102	72803	2562
512.01	2.84	5.66	1.993	428924	2102
559.41	1.42	2.73	1.923	112796	749
596.93	1.41	2.69	1.908	54059	651
610.11	20.53	1.42	0.069	10477	352
663.34	1.51	2.93	1.940	77070	800
722.90	1.61	2.97	1.845	42879	1035
847.68	1.62	3.16	1.951	46459	879
869.00	1.58	2.62	1.658	12616	411
912.11	1.44	2.96	2.056	5152	417
1015.30	1.82	3.08	1.692	6130	551
1202.12	1.89	4.53	2.397	107055	946
1461.56	1.96	5.35	2.730	22675	671
1712.96	3.01	5.73	1.904	55039	1026
1779.56	1.99	3.96	1.990	9840	538
2223.76	2.42	5.67	2.343	625697	1115
2614.85	2.25	4.34	1.929	4587	446
3424.09	86.60	139.51	1.611	373895	10291
3933.34	83.90	131.48	1.567	229592	9693
4440.61	84.91	143.97	1.696	307597	5568

Table 6.4: Various peaks with FWHM - This table shows various peaks and their FWHM. It also states the FWTM (Full Width at Tenth Maximum) and the net area of the peaks.

Doppler Broadening of 478 keV peak Recalling the process that is happening during BNCT, a neutron is captured by the ^{10}B and creates an alpha particle and an excited ^{7}Li-nucleus in 93% of the cases. When this excited ^{7}Li is returning to the ground state it emits the characteristic 478 keV γ-ray. The neutron has negligible energy compared to the reaction products, ^{7}Li and alpha. Therefore the two decay products escape in opposite directions, as seen in figure 6.10. The energy of an alpha is 1.47 MeV and therefore the energy of the ^{7}Li must be 840 keV according to the Q-values of this reaction [1]. Therefore the velocity of the the recoiling ^{7}Li-nucleus can be calculated and the Doppler shifted energy of the γ-ray is given by

$$E_\gamma = E_0 \left(1 + \frac{v(t)}{c} cos\theta\right) \tag{6.3}$$

where E_0 is the energy emitted from a stationary nucleus and θ is the angle between the nucleus velocity and the direction of the emission. (12) Thus, the recoiling ^{7}Li (Figure 6.11) nucleus is responsible for the Doppler broadening of the boron peak.

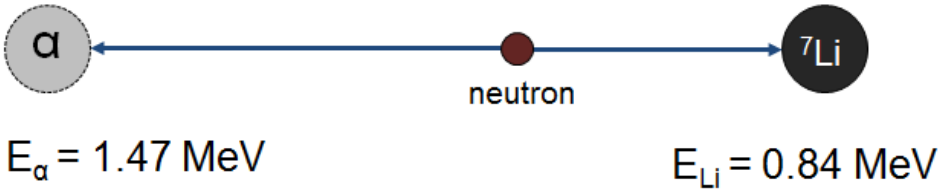

Figure 6.10: Alpha and ^{7}Li-nucleus - The neutron is assumed to be stationary as its mass (0.025 eV) is negligible compared to the reaction products. The alpha and ^{7}Li-nucleus recoil from each other with 180 degrees

[1] Q value for ground state is 2.792 MeV and for the first excited state 2.310 MeV, as the energy of the gamma ray is lost

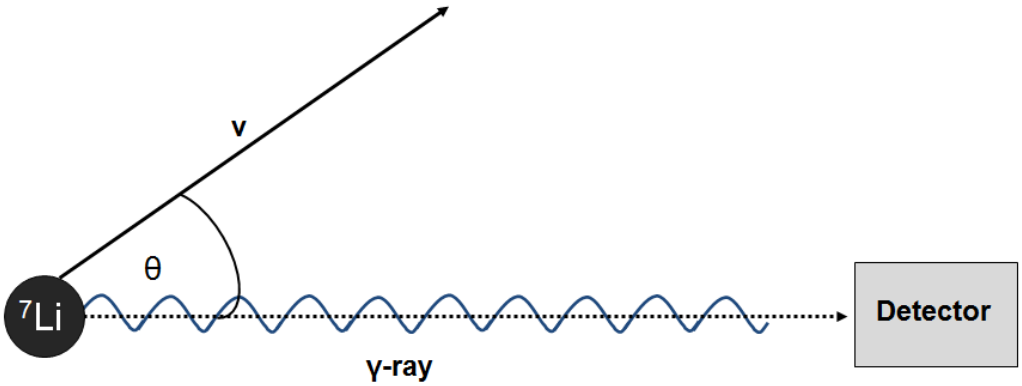

Figure 6.11: Doppler broadening due to the recoiling ^7Li-nucleus - This is an illustration of an ^7Li nucleus in flight which leads to the Doppler broadening effect

CH_2 sheet	Thermal energy		High energy	
Area $[cm^2]$	**No. of counts**	**Δ No. of counts**	**No. of counts**	**Δ No. of counts**
0	42691	1169	53398	2235
25	41929	1188	70686	2056
739.5	44270	1088	273579	2508
3009	61754	1078	462418	2337
4590	74074	1069	460497	2684
6060	92231	1169	595715	2472

Table 6.5: Number of counts in 478 keV photopeak - This table shows the number of counts and the error in the number of counts in the 478 keV photopeak for both the neutron source in thermal position and high energy position.

Analysis of 478 keV boron peak The number of counts in the 478 keV photopeak has been counted and plotted against the size of the ^{10}B containing CH_2 sheets (Figure 6.12 and 6.13).

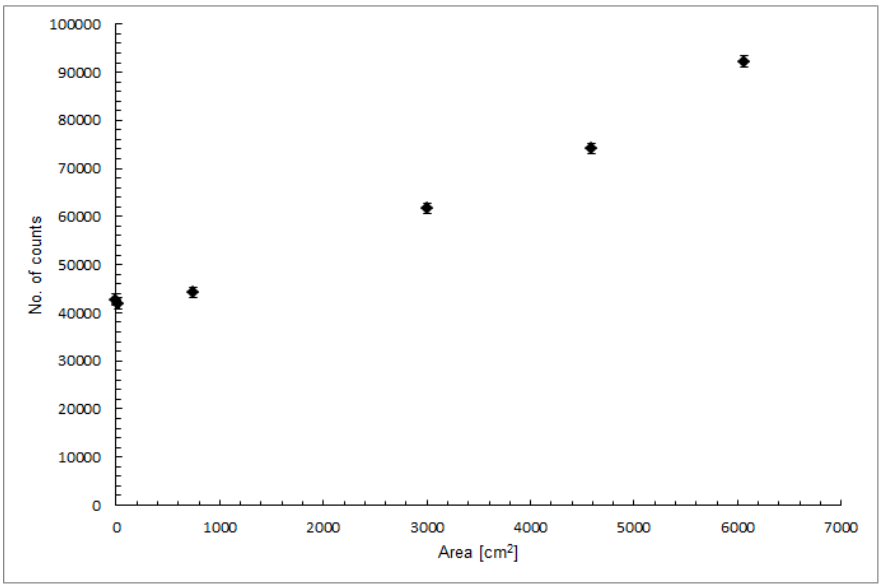

Figure 6.12: Thermal energy position - Boron Peak - This graph shows the number of counts in the boron peak against the sheet size

As figure 6.12 and 6.13 show, the number of counts increases as the sheet size is increased. This would be expected, as a larger sheet naturally contains more ^{10}B. The errors on the netcount are very small and not visible on the plots. For safety reasons,

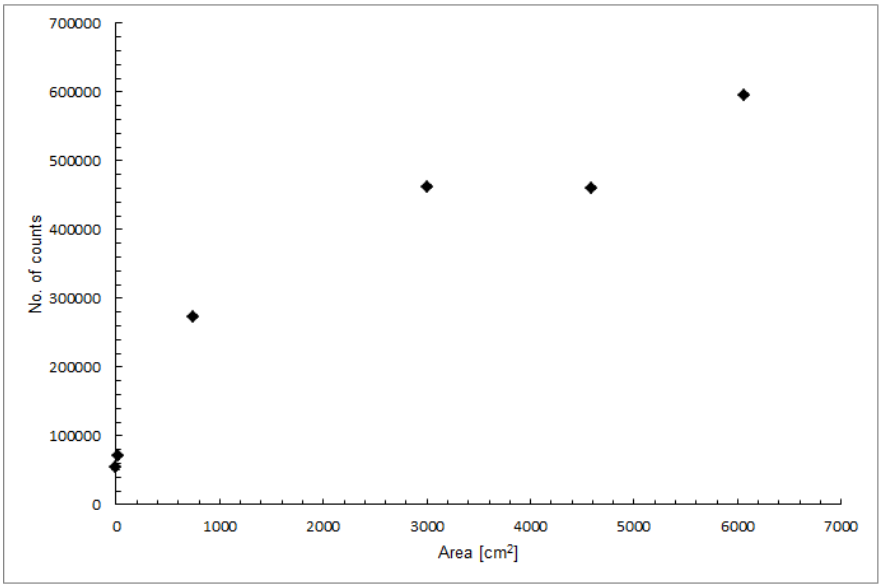

Figure 6.13: High energy position - Boron Peak - This graph shows the number of counts in the boron peak against the sheet size

another boron-containing sheet was placed behind the neutron tank. This gives rise to the number of counts in the background measurements. The sheet has not been moved throughout the experiment and has therefore contributed to each of the measurements. This additional sheet gives rise to extra uncertainties in the counting statistics.

Analysis of 2223 keV hydrogen peak The number of counts in the 2223 keV photopeak has been counted and plotted against the size of the ^{10}B containing CH_2 sheets (Figure 6.14 and 6.15).

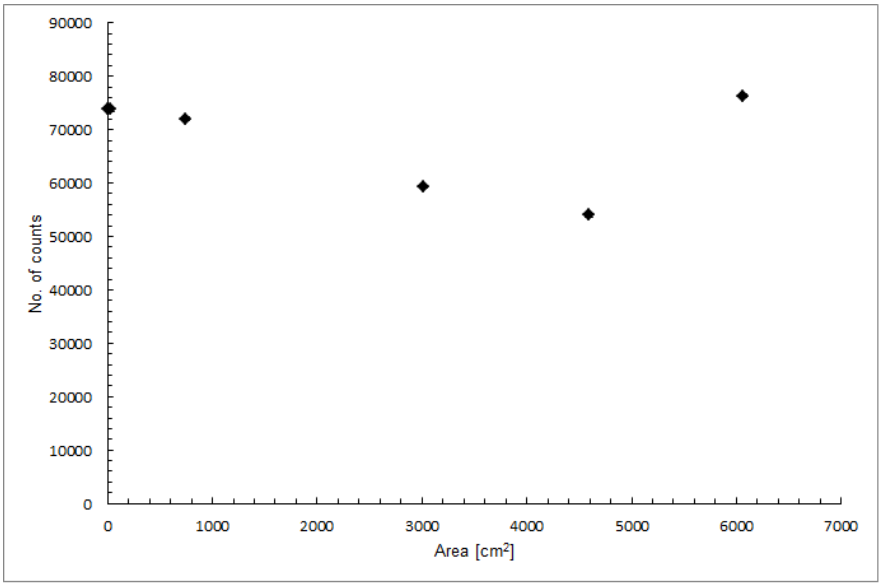

Figure 6.14: Thermal energy position - Hydrogen Peak - This graph shows the number of counts in the boron peak against the sheet size

The number of counts in the hydrogen peaks have been stated, but they are not very representative, as the plot does not seem to follow a trend. This can be explained, as there are two main contributions to the hydrogen peak. The first and main one is given by the water in the tank and the second one is given by the CH_2 sheets. The volume of the water in the tank can be approximated to $0.75mx1.25mx1m = 0.9375m^3$ and the biggest CH_2 sheet has a volume of $0.6mx1mx0.025m = 0.015m^3$. Therefore the CH_2 is only a tiny fraction, $\sim 1.6\%$, compared to the water tank and its contribution can be neglected. For a complete analysis of the number of counts, the neutron source would have to be removed from the neutron tank, which is not possible due to safety reasons. Again, the error on the netcount is too small to be visible.

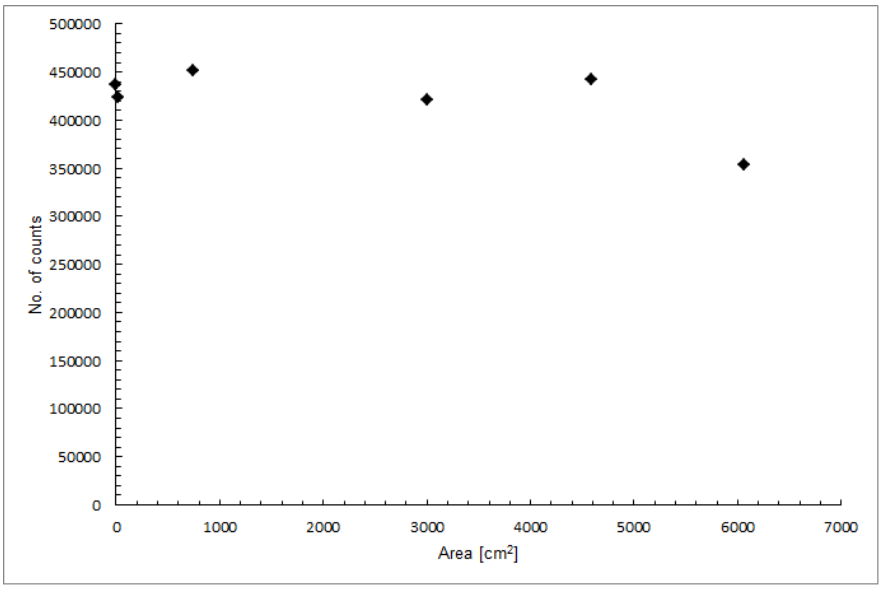

Figure 6.15: High energy position - Hydrogen Peak - This graph shows the number of counts in the boron peak against the sheet size

CH_2 sheet	**Thermal energy**		**High energy**	
Area $[cm^2]$	**No. of counts**	**Δ No. of counts**	**No. of counts**	**Δ No. of counts**
0	64904	315	353052	997
25	64966	319	359858	770
739.5	65659	323	371055	1057
3009	50845	290	368532	811
4590	46119	285	380289	850
6060	66270	353	300110	723

Table 6.6: Number of counts in 2223 keV photopeak - This table shows the number of counts and the error in the number of counts in the 2223 keV photopeak for both the neutron source in thermal position and high energy position.

6.5.2 Sodium Iodide Detector Spectra

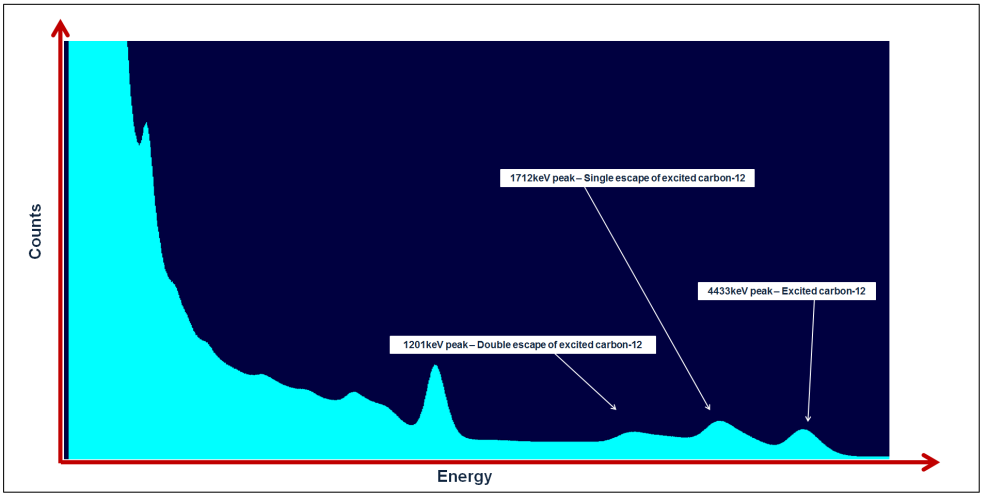

Figure 6.16: Typical Sodium Iodide spectrum - A typical spectrum collected by the Sodium Iodide detector.

A spectrum with a sodium iodide detector was collected to illustrate the advantages of the germanium detector. The boron cannot be dissolved as figure 6.16 shows. The peaks at higher energies arising from the decay of excited ^{12}C are clearly visible, and so is the hydrogen peak. The energy resolution is a lot worse than for the germanium detector, making germanium the better detector for spectroscopy.

6.5.3 Helium-3 Detector Spectra

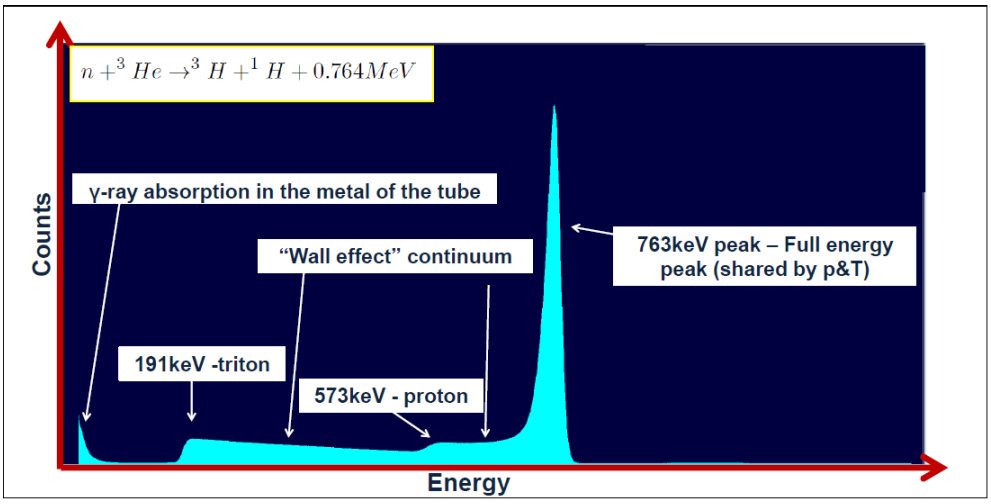

Figure 6.17: Helium spectrum - This is the helium spectrum

All spectra recorded by the Helium-3 detector have the same shape, as expected. The three peaks, corresponding to the full energy, the proton and triton are clearly visible (Figure 6.17). The features like γ-ray absorption in the tube and wall effect continuum have been described in chapter 2. In order to count the total number of neutrons, the whole spectrum was integrated. The gross area is used to calculate the neutron flux. Table 6.7 shows the number of thermal neutrons detected in 18 h in the thermal position and in the high energy position. The thermal neutron flux is a lot higher in the high energy position. This can be explained with the increasing solid angle, as the neutron source is moved towards the detector and also the increased number of thermal neutrons due to backscattering in the water of the tank. The thermal neutron flux does not change significantly with the CH_2-sheet size varied and the background flux is taken as a reference neutron flux for this setup; High energy position $\sim$ 3000 neutrons per second and in the low energy position $\sim$ 400 neutrons per second.

CH_2 sheet	**Thermal energy position**	**High energy position**
Area $[cm^2]$	**No. of counts**	**No. of counts**
0	73860	436833
25	73801	423595
739,5	72004	451056
3009	59250	421143
4590	53946	442598
6060	76349	353792

Table 6.7: Thermal neutron flux - This table shows the number of thermal neutrons detected in 18h with the ^3He detector.

6.6 Summary of Results

The experiment has shown that spectroscopy with ^{10}B is possible and the peak at 478 keV was easily identified after subtracting the background. For the smallest CH_2 sheet (5 cm x 5 cm x 2.5 cm) with 5% ^{10}B approximately 17.000 counts have been recorded in 18 h, which gives around 0.2 counts per second. The thermal neutrons emitted by the Am/Be source have been detected with the ^{3}He detector and thermal neutron fluxes of $\sim$ 3000 neutrons per second and $\sim$ 400 neutrons per second were measured in the high energy position of the source and low energy position respectively.

7

Conclusion

For the evaluation of Compton camera imaging during Boron Neutron Capture Therapy, various GAMOS simulations and an experiment in the neutron laboratory have been performed. In the simulations the image quality for the reconstruction of a 478 keV γ-ray source equivalent to the radiation emitted during BNCT was investigated. The Compton camera setup was subsequently optimised for this energy. In the experiment, a boron containing material was exposed to a neutrom beam and the 478 keV was measured and analysed. Furthermore the thermal neutron flux was estimated.

The simulations with GAMOS showed that the optimum Compton camera imaging system would consist of two germanium detectors used as scatter and analyser detector with optimum thicknesses of 10 mm and 90 mm respectively. For economic reasons, a 40 mm thick analyser detector is assumed to be sufficient. Utilising events from these multiple interactions by employing advanced event processing and image reconstruction techniques will possibly improve the overall imaging of the optimised Compton camera configuration significantly, as the single/single interactions, which are the easiest to process and reconstruct only account for a small fraction of all events. Furthermore the study of different detector materials, which could eventually increase the efficiency, is recommended. After the optimisations have been taken into account, a flux of 100,000 γ-ray delivers around 100 cones, which is sufficient for a good image reconstruction.

The experiment in the neutron laboratory has shown that spectroscopy with the 478 keV photopeak is possible and the peak can be clearly separated from background.

The results of the GAMOS simulations and boron spectroscopy and neutron detection can be combined to scale the number of counts in the boron peak in a realistic BNCT treatment case. Two main assumptions have to be made: Firstly, a $10^{12}\frac{n}{s}$ neutron beam generator, like the one used in Birmingham, will increase the number of neutrons by 10^9 compared to the Am/Be neutron source used during this project. This leads to a greater ^{10}B capture in the target and hence an increase in the number of γ-rays. Secondly, during treatment, the germanium detector will be placed next to the patient, which significantly increases the solid angle coverage.

By taking these assumptions into account, the number of counts can be increased from around 20,000 in a 5 cm x 5 cm x 2.5cm ($= 62.5cm^3$) volume in the boron peak to 160,000,000 in 18h or from 0.2 $\frac{counts}{second}$ to 1860 $\frac{counts}{second}$ respectively. It has been shown that roughly 100,000 γ-rays are needed to create 100 cones, which is sufficient for a good image reconstruction. Hence, it would take about 1 min to collect enough γ-rays. However, the concentration of boron in the patient's body is significantly lower; 0.0052% in the tumour, compared to 5% in the CH_2-sheet used in the experiment. Therefore, it would take roughly 5,000 seconds (about 1.5h) to collect enough counts in the $62.5cm^3$ volume.

Furthermore, for a $1cm^3$ volume, which would be desirable during treatment, a total of about 100 h would be required to collect sufficient amount of γ-rays. Thus, in order for the Compton camera system to be viable in producing an image of the region being treated, a higher yield of cones for a given number of γ-rays will be required. To improve the efficiency of the Compton camera system, the solid angle between the patient and the scatter detector should be minimised. Ideally the system would have a torus shape, which could be placed around the patient's head. Additionally the area of the absorber detector should be larger than the area of the scatter detector to maximise the solid angle coverage between the two detectors. This should be investigated in the future and the GAMOS simulations have to be validated with an experiment.

Appendix A

GAMOS Codes

A.1 GAMOS - Input file

```
/run/verbose 1
/control/verbose 1
/run/verbose 1
/tracking/verbose 0
/gamos/generator GmGenerator
#/gamos/userAction GmCountProcessesUA
#/gamos/userAction GmHistosGammaAtSD
#/gamos/userAction GmHitsHistosUA
#/gamos/userAction GmRecHitsHistosUA
/gamos/setParam CC:EvtClass:GammaEnergy 478.*keV
/gamos/setParam CC:EvtClass:PhotopeakEPrec 0.02
#/gamos/setParam CC:EvtClass:ComptonRecHitDistScat 0.*mm
#/gamos/setParam CC:EvtClass:ComptonRecHitDistAbs 0.*mm
/gamos/setParam CC:EvtClass:DumpEvent 1
/gamos/setParam GmGeometryFromText :FileName 5mm+sp1_0_0_105.geom
/gamos/geometry GmGeometryFromText
/gamos/physicsList GmEMPhysics
/gamos/GmPhysics/addPhysics gamma-lowener
/gamos/GmPhysics/addPhysics electron-lowener
/gamos/setParam CC:EvtClass:DumpSingles 1
```

```
/gamos/setParam CC:EvtClass:DumpMultiples 0
#/gamos/setParam CC:EvtClass:1stHitAlgorithm NM1stHitByEnergy
#/gamos/setParam CC:EvtClass:1stHitAlgorithmFirst NM1stHitByEnergy
#/gamos/setParam CC:EvtClass:1stHitAlgorithmSecond NM1stHitByEnergy
/gamos/setParam CC:EvtClass:CoincidenceTime 200.*ns
/gamos/userAction CCEventClassifierUA
/run/initialize
/gamos/setParam SD:EnergyResol:Scatterer 0.01
/gamos/setParam SD:EnergyResol:Absorber 0.01
/gamos/setParam SD:RecHit:MinimumEnergyBehaviour:Scatterer AcceptIf1Big
/gamos/setParam SD:RecHit:MinimumEnergy:Scatterer 5.*keV
/gamos/setParam SD:RecHit:MinimumEnergyBehaviour:Absorber AcceptIf1Big
/gamos/setParam SD:RecHit:MinimumEnergy:Absorber 5.*keV
/gamos/setParam SD:MeasuringTime:Scatterer 5.e-6*s
/gamos/setParam SD:MeasuringTime:Absorber 5.e-6*s
/gamos/setParam SD:DetUnitID:NAncestors 2
#/gamos/SD/assocSD2LogVol GmSDSimpleExactPos Scatterer scatcrystal
/gamos/SD/assocSD2LogVol GmSDSimple Scatterer scatcrystal
/gamos/recHitBuilder GmRecHitBuilder1to1 Scatterer
#/gamos/SD/assocSD2LogVol GmSDSimpleExactPos Absorber abscrystal
/gamos/SD/assocSD2LogVol GmSDSimple Absorber abscrystal
/gamos/recHitBuilder GmRecHitBuilder1to1 Absorber
/gamos/generator/addSingleParticleSource source gamma 478.*keV
/gamos/generator/timeDist source GmGenerDistTimeDecay 3.264e-6*curie
/gamos/generator/directionDist source GmGenerDistDirectionRandom
#/control/execute /local/dsj/GAMOS/GAMOS.3.0.0/examples/visVRML2FILE.in
#/run/beamOn 20
/run/beamOn 70000000
```

A.2 GAMOS - Geometry file

#include /local/dsj/GAMOS/GAMOS.3.0.0/data/NIST_elements.txt
#include /local/dsj/GAMOS/GAMOS.3.0.0/data/PET_materials.txt
#include /local/dsj/GAMOS/GAMOS.3.0.0/data/NIST_materials.txt
// rotation matries
:ROTM RM0 90 0 90 90 0 0
:ROTM RM1 0 90 0
:ROTM RM2 0 0 0
//— World
:VOLU world BOX 200. 125. 125. G4_AIR

// ——————- Scatterer ——————————————————————————
:P NSCATCRYSTALS_transaxial 12 // number of crystals in each block, transaxial direction
:P NSCATCRYSTALS_axial 12 // number of crystals in each block, axial direction
:P SCATCRYS_transaxial 0.5*cm // transaxial crystal dimension
:P SCATCRYS_axial 0.5*cm // axial crystal dimension
:P SCATCRYS_radial 0.5*cm // radial crystal dimension
:PS SCATCRYS_MATE G4_Ge // crystal material

//— Block of crystals———————————
:P SCATBLOCK_X
$SCATCRYS\_radial$
: $PSCATBLOCK\_Y$
SCATCRYS_transaxial*
$NSCATCRYSTALS\_transaxial$
: $PSCATBLOCK\_Z$
SCATCRYS_axial*
$NSCATCRYSTALS\_axial$
: $VOLUscatblockBOX$
SCATBLOCK_X/2.
$SCATBLOCK\_Y$/2.

SCATBLOCK_Z/2. G4_AIR
:PLACE scatblock 1 world RM2 52.5 0. 0.

//— Crystals——-
:VOLU scatcrystal BOX
$SCATCRYS\_radial/2.$
SCATCRYS_transaxial/2.
$SCATCRYS\_axial/2.$
SCATCRYS_MATE
:PLACE_PARAM scatcrystal 1 scatblock SQUARE_YZ RM0
$NSCATCRYSTALS\_transaxial$
NSCATCRYSTALS_axial
$SCATCRYS\_transaxial$
SCATCRYS_axial
-(
$NSCATCRYSTALS\_transaxial - 1)/2. *$
SCATCRYS_transaxial -(
$NSCATCRYSTALS\_axial - 1)/2. *$
SCATCRYS_axial

// ——————- Absorber ——————————————————————

:P NABSCRYSTALS_transaxial 12 // number of crystals in each block, transaxial direction
:P NABSCRYSTALS_axial 12 // number of crystals in each block, axial direction
:P ABSCRYS_transaxial 0.5*cm // transaxial crystal dimension
:P ABSCRYS_axial 0.5*cm // axial crystal dimension
:P ABSCRYS_radial 2.0*cm // radial crystal dimension
:PS ABSCRYS_MATE G4_Ge // crystal material

//— Block of crystals————
:P ABSBLOCK_X
$ABSCRYS\_radial$
: $PABSBLOCK\_Y$

ABSCRYS_transaxial*
NABSCRYSTALS_transaxial
: *PABSBLOCK_Z*
ABSCRYS_axial*
NABSCRYSTALS_axial
: *VOLUabsblockBOX*
ABSBLOCK_X/2.
ABSBLOCK_Y/2.
ABSBLOCK_Z/2. G4_AIR
:PLACE absblock 1 world RM2 95. 0. 0.

//— Crystals————-
:VOLU abscrystal BOX
$ABSCRYS_radial/2.
$ABSCRYS_transaxial/2.
$ABSCRYS_axial/2.
$ABSCRYS_MATE
:PLACE_PARAM abscrystal 1 absblock SQUARE_YZ RM0
NABSCRYSTALS_transaxial
NABSCRYSTALS_axial
ABSCRYS_transaxial
ABSCRYS_axial
-(
$NABSCRYSTALS_transaxial-1)/2.*
$ABSCRYS_transaxial -(
$NABSCRYSTALS_axial-1)/2.*
$ABSCRYS_axial

References

[1] G. Gilmore and J. Hemingway. *Practical gamma-ray spectrometry*. John Wiley & Sons Ltd, 1st edition, 1995.

[2] Knoll. *Radiation Detection And Measurement*. Wiley, 4th edition, 2010. 7, 8, 11, 26, 71

[3] J. H. Lee and C. S. Lee. **Studies on sensitivity, resolution, and Doppler broadening in gamma-ray imaging with pixellated semiconductor detectors**. *Elsevier*, pages 639c–642c, 2004. Nuclear Physics A. 30

[4] L. Harkness. *A Design Study of the Semiconductor Sensor Head for the ProSPECTus Compton Camera*. PhD thesis, University of Liverpool, July 2010. 7, 28, 31

[5] A. N. et al Grint. **Compton Camera - SPECT Medical Imaging Application**. *University of Liverpool*, 2010. 30

[6] G. Kimminau and S.l Cleverley. **Market Opportunity Assessment and target approach for a new radiation imaging camera system**. *Isis Enterprise*, 2011.

[7] L. Harkness. **ProSPECTus - A look into future SPECT/MRI imaging**. *University of Liverpool*, 2011.

[8] T. W. Crane and M. P. Baker. **Neutron Detectors**.

[9] F. Quarati. **Studies and implementation of $LaBr_3$ and $LaCl_3$ scintillator detectors**. *eesa SCIENCE*, October 2006. Gamma Ray Scintillator Development Project.

[10] M. Cortesi. **A Suggestion for ^{10}B Imaging During Boron Neutron Capture Therapy**. *Department of Physics of the University and INFN, Milan, Italy.*

[11] M. K. Kubo and Y. Sakai. **A Simple Derivation of the Formula of the Doppler Broadened 478 keV - Ray Lineshape from ^{7*}Li and Its Analytical Application**. *Journal of Nuclear and Radiochemical Sciences*, **1**(2):83–85, December 2004.

[12] Jung N. S. Choi, H. D. and B. G. Park. **Analysis of Doppler broadened peak in thermal neutron induced $^1 0B(n, \alpha\gamma)^7 Li$ reacion using hypogam**. *Nuclear Enginieering and Technology*, **41**(1):83–85, February 2009. Department of Nuclear Engineering, Seoul National University. 78

[13] S. Green. **Binary therapies in the treatment of cancer**. *University of Birmingham*, January 2010. STFC Innovations Birmingham. 3

[14] C. Oestlund. *BNCT in vivo dosimetry: A feasibility study using an HPGe detector for prompt gamma spectroscopy*. PhD thesis, Lund University - Medical Radiation Physics - Clinical Sciences, 2005.

[15] A. Hamed and A. M. Hassan. **ESTIMATION OF BORON IN SOME LOCAL MATERIALS BY PROMPT GAMMA RAY NEUTRON ACTIVATION ANALYSIS TECHNIQUE**. *Proceedings of the 2^{nd} Environmental Physics Conference*, February 2006. STFC Innovations Birmingham.

[16] B. Bruyneel. *Characterization of Segmented Large Volume, High Purity Germanium Detectors*. PhD thesis, Universitaet zu Koeln, June 2006.

[17] International Atomic Energy Agency. **Current Status Of Neutron Capture Therapy**. *IAEA*, 2001.

[18] A. et al Valda. **Development of a Tomographic System for Online Dose Measurements in BNCT (Boron Neutron Capture Therapy)**. *Brazilian Journal of Physics*, **35**(3b):785–788, September 2005.

[19] I. et al Murata. **Feasibility study on BNCT-SPECT using a CdTe detector**. *Progress in NUCLEAR SCIENCE and TECHNOLOGY*, **1**:267–270, 2011.

[20] D. M. et al Minsky. **ESTIMATION OF BORON IN SOME LOCAL MATERIALS BY PROMPT GAMMA RAY NEUTRON ACTIVATION ANALYSIS TECHNIQUE**. *Proceedings of the 2^{nd} Environmental Physics Conference*, February 2006. STFC Innovations Birmingham.

[21] S. et al Watanabe. **A Si/CdTe Semiconductor Compton Camera**. *SLAC-PUB-11144*, April 2005. 30

[22] W.L. Dunn and R. P. Hugtenburg. **The Interaction of Radiation with Matter: Charged Particle and Electron Interactions**. *IEEE Short Course*, October 2006. 11

[23] P. Rinard. **Neutron Interaction with Matter)**. *Nuclear Regulatory Commission*, page 357ff, March 1991. Passive Nondestructive Assay of Nuclear materials.

[24] W.F Verbakel. **Validation of the scanning -gamma-ray telescope for in vivo dosimetry and boron measurements during BNCT.** *Phys Med Bio*, **46**:3269–85, December 2001.